2013

In-plane structural and electronic anisotropy of iron-based superconductors

Erick Blomberg
Iowa State University

In-plane structural and electronic anisotropy of iron-based superconductors

by

Erick Blomberg

A dissertation submitted to the graduate faculty

in partial fulfillment of the requirements for the degree of

DOCTOR OF PHILOSOPHY

Major: Condensed Matter Physics

Program of Study Committee:

Ruslan Prozorov, Major Professor

Andreas Kreyssig

Jim Cochran

Mani Mina

Edward Yu

Iowa State University

Ames, Iowa

2013

DEDICATION

I dedicate this work to my family. In spite of my childhood science projects ruining the carpet, setting the house on fire, and blowing out windows, my family never stopped encouraging me to pursue my love of tinkering and scientific experimentation.

TABLE OF CONTENTS

LIST OF TABLES

LIST OF FIGURES

ACKNOWLEDGEMENTS

I would like to thank everyone who made this work possible. That list is quite long, but I would like to acknowledge a few specific individuals here:

First and foremost I would like to thank Ruslan Prozorov and Makariy Tanatar for advising me through my doctoral work. They have been invaluable in preparing me for a career as a scientist. Without them this thesis would never have been possible.

I would also like to thank my entire research group for making our lab a productive and friendly environment. Specifically I want to thank, Jacob Hoberg and Plengchart Prommapan for their collaboration in developing polarized optical imaging techniques. Ryan Gordon, Kyuil Cho, Catalin Martin and Hyunsoo Kim were invaluable for discussions on superconductivity, phase diagrams, and data interpretation. Jason Murphy and Nicholas Spyison were a great resource for while I was developing new instrumentation. I want to thank Vikas Malik, Charles Strehlow, and Steve Yeninas for useful discussions ranging from physics to typesetting and preparing talks.

Ouside the lab, I enjoyed many physics discussions with Arun Madhavan, Ben Blomberg and Mark Blomberg. These conversations, often over pizza and beer, always reminded me why I chose to pursue a doctorate in physics. I also owe a huge debt of gratitude to my entire family for their endless encouragement.

I would like to thank the research group of Alan Goldman for their help with structural studies. I especially want to thank Andreas Kreyssig for the time he invested in helping me with X-ray experiments as he was the most influential person on my doctoral research after my advisors.

Excellent single crystals were supplied by the research groups of Paul Canfield and Hai-Hu Wen. Specifically I want to thank Ni Ni, Alex Thaler, Sheng Ran, Rongwei Hu, and Sergey Bud'ko within the Canfield group and Bing Shen in the Wen group.

I would like to thank Warren Straszheim for performing chemical characterization of samples.

Finally, I would like to thank Jörg Schmalian, Igor Mazin, and Michelle Johannes and especially Rafael Fernandes for theoretical support of my research and useful discussions.

ABSTRACT

Many iron-based superconductors undergo a tetragonal to orthorhombic change of their crystallographic lattice symmetry, as well as paramagnetic to anti-ferromagnetic ordering upon cooling through a characteristic temperature T_N. The anisotropic structure of the orthorhombic crystal symmetry would naturally lead one to expect to find in-plane electronic anisotropy.

Upon cooling through T_s, and going into the orthorhombic symmetry, crystals divide into many small *twin domains*. Although crystallographically identical, the twin domains express four different rotations of the orthorhombic lattice within the **ab**-plane making direct measurements along an individual orthorhombic axis impossible. This complication lead to the developement of uniaxial stress and strain detwinning, which makes one of the four domain rotations far more energetically favorable than the other three, to the extent that more than 90% of the entire crystal volume may be represented by the dominant domain. Once in this *detwinned* state, measurements may be made along the individual orthorhombic axes, allowing one to probe in-plane anisotropy.

Following the developement of the detwinning technique, measurements of the in-plane resistivity anisotropy between the orthorhombic a_o and b_o axes were made. The results, however, turned out to be the opposite of what is predicted from simple models of electrical resistivity. Many different competing theories were developed to understand this unusual behavior. The goal of my doctoral research is to understand the validitiy of these different theories and discover the primary driving force behind this unexpected result.

My experiments on the effects of doping on the in-plane resistivity anisotropy yielded

an interesting result that not only is there an assymetry between electron and hole doping, but also that the sign of the anisotropy changes sign with sufficient hole doping. This result, along with the tempreature dependence of the in-plane resistivity anisotropy, provide very strong evidence that the primary source is anisotropic scattering due to magnetic spin fluctuations.

CHAPTER 1. Introduction

1.1 Motivation

Electrical resistance has a profound effect on our daily lives whether or not it is immediately obvious. As an electrical current passes through any imperfect conductor, energy is lost in the form of heat. This loss not only has a monetary cost, but also places limitations on the capabilities of all systems which rely on electrical power. For example the U.S. Office of Electricity Delivery and Energy Reliability estimates that nearly 7% of all electrical power, generated in the US, is lost in transmission between the power plant and the consumer. For a typical high tension power line, the loss per mile of transmission carries a monetary cost of over $1.03 million and an environmental cost of more than 2.7 million pounds of carbon emissions [1]. These losses are not limited to electrical transmission. Electrical appliances themselves also suffer from the same loss, creating further waste. Additionally power losses also create technical limitations ranging from the speed of computer processors to the time between recharging portable electrical devices.

The reasons above clearly demonstrate the value in finding ways to reduce energy waste. There are many ways to reduce energy waste, but one particularly promising candidate is a class of materials called *superconductors*.

In 1908, physicist, Heike Kamerlingh Onnes succeeded in liquefying helium [2], allowing him to reach colder temperatures than had ever previously been achieved and began a rigorous study of the properties of very pure metals at low temperatures. In 1911,

Onnes made the startling discovery that, at temperatures below 4.2 K, mercury ceased to show any electrical resistance [3]. Onnes had discovered the first *superconductor*, a material with no electrical resistance allowing electricity to flow without loss. Shortly thereafter other materials were discovered to be superconducting such as lead at 7 K [4] and niobium at 9.3 K [5]. As time went on, many more superconducting compounds were discovered.

No doubt, these materials are of great interest because of their potential use in both power transmission and electrical devices as they have no electrical resistivity and consequently have absolutely no energy losses. Although superconductors are used in some specialized applications today, there are techincal limitations preventing them from them being used broadly.

Superconductivity is already in use in modern technology. Current applications include magnetic levitation in maglev trains, RF filters in cell phone base stations, and magnets used in medical imaging systems such as MRI, not to mention applications in highly specialized scientific instruments. Unfortunately superconductivity is currently only used in very specialized applications as the necessary temperatures are still very low compared to ambient temperatures. The highest temperature superconductor to date is $HgBa_2Ca_2Cu_3O_x$ [6] which superconducts at temperatures up to 133 K, which is still 160 K below room temperature. Although such temperatures can easily be reached with liquid nitrogen (77 K), these materials are complicated to produce and are brittle ceramics lacking the malleability we normally associate with metal wires, making them difficult to integrate into real world applications.

Many scientists would argue that the Holy Grail of current condensed matter physics and materials science research is the development material which superconducts at ambient temperature and pressure. Although this goal is likely still many years away, it has motivated over 100 years of superconductivity research which is ongoing today.

At this point we still don't have enough of an understanding of superconductivity

to even predict which materials are superconducting. For this reason it is important to explore every possible facet of superconductivity and superconductors themselves. Unfortunately these facets are often intertwined and require study from many different experimental angles to disentangle the individual effects. Consequently the discovery of a new superconducting material generates a flurry of excitement and new research. In 2008, a new class of superconductors, based on iron, was discovered [7] and became the primary interest of this work.

This work focuses on studying in-plane anisotropic properties, primarily in the normal (non-superconducting) state, but in close proximity to superconductivity in iron-based superconductors. These anisotropic properties provide an interesting oppourtunity to study the effects variation of a parameter within an individual sample which may therefore be interpreted much more directly because of the smaller number of effects which must be disentangled.

1.2 The Twin Domain Problem

Crystal *twinning* is a property where two separate crystals share lattice points. This causes an intergrowth of crystallographically identical *twin domains* but with different orientations. The size of individual domains varies widely depending on the material. Selenite crystals with twin domains as large as 14 metres have been discovered in the famous Naica Mine, in northern Mexico. By comparison pyrite often forms centimeter size twin domains, while granite exhibits domains that can only be seen under a microscope.

The existence of twin domains can be problematic because many experimental measurements become infeasible without single crystals of a minimum practical size. For example neutron diffraction and resistivity measurements become nearly impossible for crystals with sub-milimeter dimensions. The iron-based superconductors exhibit spontaneous twin domain formation after undergoing a tetragonal to orthorhombic phase tran-

Figure 1.1 A pyrite crystal with simple penetration twinning of three cubic domains.

sition. These twin domains have micrometer widths which make some measurements impossible.

The twin domain problem is, however, not unique to iron-based superconductors. The intensly studied cuprate superconductors also exhibit a tetragonal to orthorhombic transition which causes the spontaneous developement of micrometer size domains. This situation is quite different however, as the transition occurs well above room temperature in copper-oxide superconductors (for example the transition occurs around 450 ^{o}C in $YBa_2Cu_3O_{7-\delta}$).

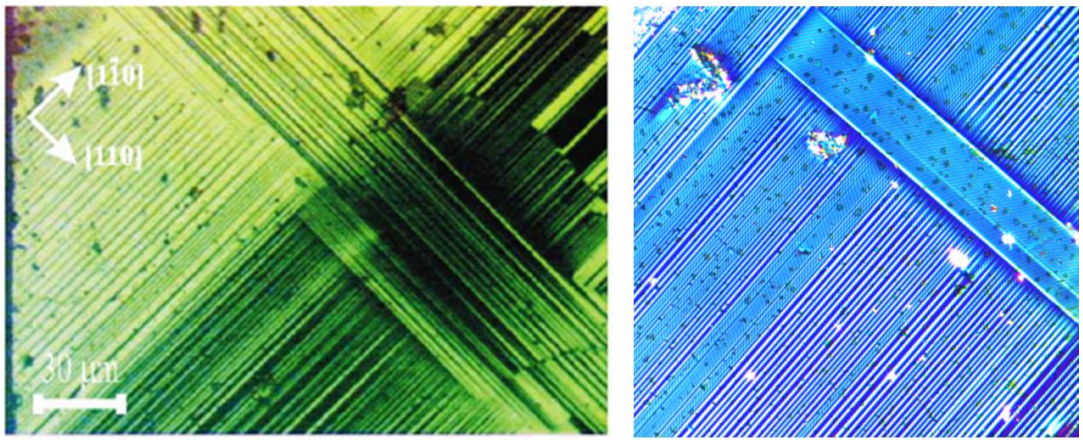

Figure 1.2 Polarized microscopy images of $YBa_2Cu_3O_{7-\delta}$ (left) and $CaFe_2As_2$ (right), well below T_N. The colored stripes are twin domains, which are crystallographically identical, but with different in-plane rotation angles. Both materials undergo a tetragonal to orthorhombic structural transition which leads to the formation of twin domains.

Various techniques were developed to eliminate twin domains, in the cuprates to allow experiments to be performed on large, truely single domain, crystals. The most simple of which is to exert uniaxial stress on a twinned crystal [8] which makes one domain orientation more energetically favorable than the others. After a stress of approximately 25 MPa was applied, the crystal would become *detwinned*, and remain as a single domain crystal after the stress was released.

Detwinning $YBa_2Cu_3O_{7-\delta}$, and the cuprates in general, is a much simpler situation than it is for the family of iron-based superconductors. In the cuprates, the structural transition is well above room temperature which means uniaxial force detwinning can be performed in ambient conditions. For iron-based superconductors however, the transition temperatures range from 100-200 ^{o}C below room temperature which means that detwinning must be performed in a cryogenic environment and imposes a host of technical challenges. A major part of this thesis was overcoming those challenges which is discussed at length in Chapter 3.

CHAPTER 2. Iron-based superconductors

2.1 Introduction

In 2006 superconductivity was discovered in LaFeOP by Y. Kamihara *et al.* [9]. This was the first discovery of superconductivity in an iron-based superconductor. Although it was novel, the transition temperature was found to be rather low at 3.2 K which is even lower than many pure elemental superconductors (for example, lead superconducts at 7 K), and consequently did not generate much excitement.

In 2008, the same group of researchers found that flourine doping of LaFeAsO could achieve superconducting transition temperatures as high as 26 K [7]. This was the first of the RFeAsO (R=rare earth) family of superconductors, commonly denoted as the "1111" system, and displayed transition temperatures up to 55K. With 30 K generally being considered the threshold for classification as a high temperature superconductor, this new result generated immediate interest. This set into motion an explosion of research into iron-based superconductors.

This led to the search for other materials containing FeAs layers with Fe atoms in a square planar lattice arrangement, similar to the RFeAsO "1111" system. Among the FeAs layered compounds which displayed superconductivity were the AFeAs "111" and $A\mathrm{Fe_2As_2}$ "122" systems (A=alkali earth for both systems).

Although the "122" system has only displayed a maximum T_c of 38 K, the system is particularly interesting because of the coexistence of superconductivity and magnetism over a broad range of the phase diagram especially considering that magnetism generally

supresses superconductivity. This system also has an advantage over other systems in that it produces comparatively much larger single crystals which are invaluable for measurments such as neutron scattering and in-plane anisotropy measurements (discussed in detail below). For these reasons the "122" system is the primary focus of this work.

2.2 $A\mathbf{Fe_2As_2}$ Properties ($A = Sr, Ba, Ca, Eu$)

2.2.1 Crystallographic Structure

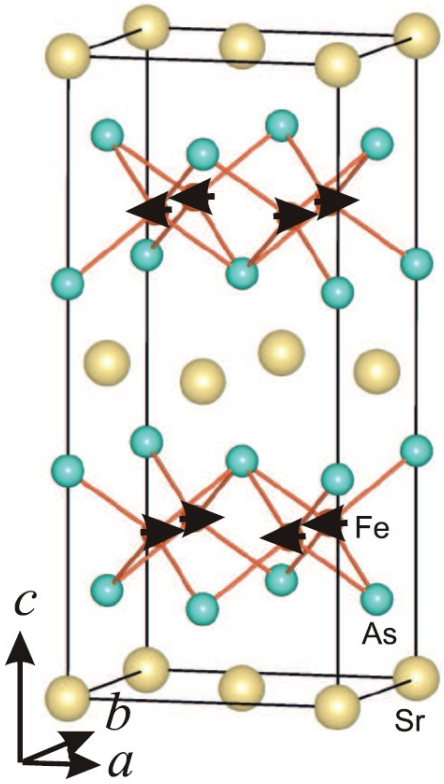

Figure 2.1 Crystallographic structure of $SrFe_2As_2$ (identical to the $ThCr_2Si_2$ structure), common for the entire "122" family of iron-based superconductors. The black arrows represent the Fe atoms and their magnetic ordering directions (discussed in detail below). Image from J. Lynn and P. Dai, Physica C 469, 469 (2009)

The crystal structure of the "122" family of iron-based superconductors, Fig. 2.1, consists of alternating FeAs layers separated by alkali earth layers forming a body-centered-

tetragonal structure (space group I4/mmm) at room temperature [11; 12; 13]. The alkali earth layers are arranged in a square lattice within the ab-plane and are the center of a distorted tetrahedron of As atoms. In the tetragonal symmetry the $\mathbf{a}_T$ and $\mathbf{b}_T$ - lattice vectors are equal in length.

Upon cooling through a characteristic (see Table 2.1) structural transition temperature, T_s, the crystal undergoes a symmetry lowering to a face-centered-orthorhombic (space group Fmmm) crystal symmetry. In the orthorhombic phase the lattice vectors in the ab-plane are no longer equal with $\mathbf{a}_O > \mathbf{b}_O$.

Table 2.1 Properties of AFe$_2$As$_2$ Parent Compounds

Material	(T_s)	$\mathbf{a}_o/\mathbf{b}_o$ (10 K)	Ref.
$BaFe_2As_2$	135 K	1.007	[15]
$CaFe_2As_2$	170 K	1.013	[16]
$EuFe_2As_2$	190 K	1.006	[17]
$SrFe_2As_2$	201 K	1.011	[18]

2.2.2 Magnetic Ordering

In the "122" fmaily of iron-based superconductors, the structural transition is accompanied by magnetic ordering of magnetic moments of the iron atoms. At room temperature the moments are randomly oriented. Upon cooling through a characteristic temperature, T_N, the moments undergo a Néel transition to antiferromagnetic (AFM) ordering [16]. In the parent compounds $T_s = T_N$.

The magnetic ordering below T_N is "stripe" type AFM order, illustrated in in Fig. 2.2. The iron moments align parallel to the longer, a_o, orthorhombic axis, forming magnetic "stipes" parallel to the b_o-axis. The moment direction alternates between being parallel and anti-parallel to the a_o-axis as one moves along the a_o- or c_o-axes.

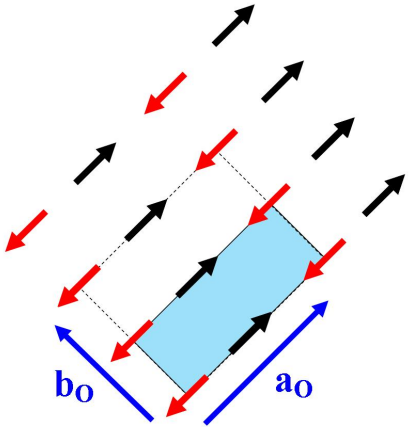

Figure 2.2 Stripe type antiferomagnetic (AFM) ordering in $A\mathrm{Fe_2As_2}$ superconductors. In the antiferromagnetically ordered state, the iron moments are aligned parallel to the longer, a_o, orthorhombic axis, forming magnetic "stipes" parallel to the b_o-axis. Moment directions alternate as one moves along the a_o- and c_o-axes. The black dashed line indicates the orthorhombic (structural) unit cell while the shaded blue area indicates the magnetic unit cell.

2.2.3 Doping Phase Diagrams

The "122" family of iron-based superconductors have a rich phase diagram upon doping, by chemical substitution, of both the alkali earth site as well as the iron site. Early investigations suggested that $BaFe_2As_2$ had similarities to $LaFeAsO$ which suggested it might be an excellent candidate for serving as a parent compound for oxygen-free iron-arsenide based superconductors [10] with the $ThCr_2Si_2$, "122" structure. Soon after experimental investigations found that indeed, doping at either site may induce superconductivity.

Isostructural KFe_2As_2 was known to exist since the 1980's [14]. This knowledge, coupled with the fact that Ba^{2+} and K^+ have a similar ionic radius (0.217 $vs.$ 0.227 nm) made potassium an excellent candidate for hole dopping $BaFe_2As_2$ on the barium site. Superconductivity was readily discovered in $Ba_{1-x}K_xFe_2As_2$ with T_c up to 38 K, at an optimal doping of 40% potassium [19].

Doping of the iron site is represented by form $A(Fe_{1-x}T_x)_2As_2$ with A=alkali earth

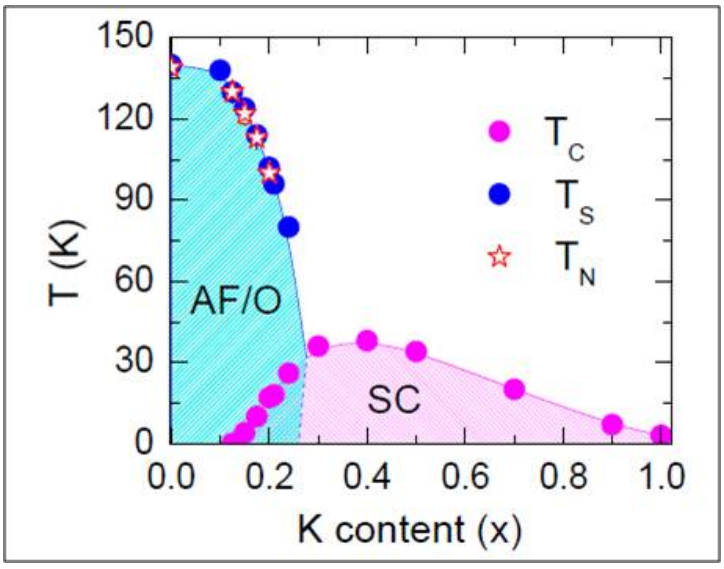

Figure 2.3 Temperature *vs.* doping phase diagram for $Ba_{1-x}K_xFe_2As_2$. Both AFM ordering and the tetragonal to orthorhombic phase transition are suppressed upon doping. Sufficient doping induces superconductivity.Superconductivity and magnetism coexist until nearly optimal doping. Superconductivity extends out to 100% potassium substitution of the barium site.

and T=transition metal (disccusion in this work is primarily T=Co, Ni, Ru) where x represents the fraction of chemical resubstitution. Bulk superconductivity induced by electron doping in the "122" family of compounds was first reported for $Ba(Fe_{0.9}Co_{0.1})_2As_2$ with T_c=22 K[23]. Soon after a detailed study of the Co dopping vs. temperature was peformed [20] and revealed a superconducting dome beginning around x=0.04, and terminating around x=0.12. It was also discovered that the structural transition, T_S, and magentic ordering temperatures, T_N are suppressed by roughly 15 K for every 1% iron substitution by cobalt.

2.3 Twin Domains

2.3.1 Types of Twins

Mineralogists have studied crystal twinning for over a century for it's value in identifying and classifying minerals. Mineralogy textbooks generally define crystal twins as

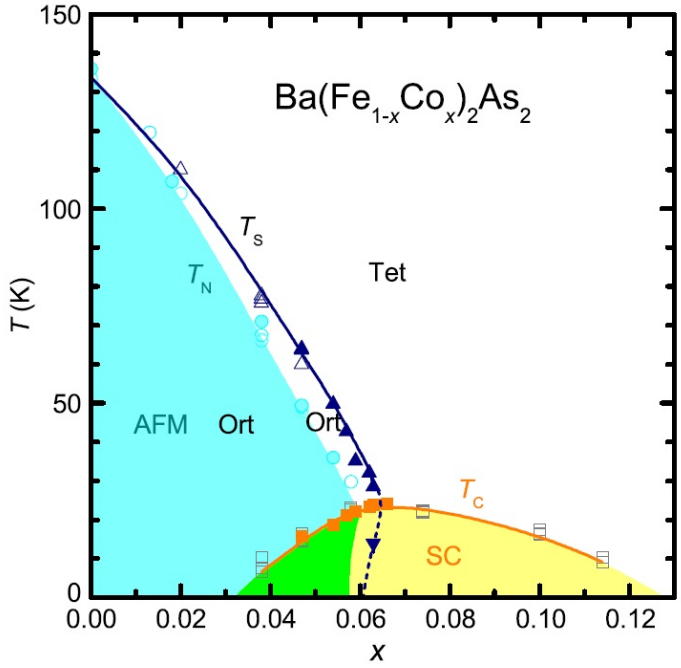

Figure 2.4 Phase diagram for $Ba(Fe_{1-x}Co_x)_2As_2$. Increasing Co substitution of Fe suppresses the structural transition and magnetic ordering temperatures, while forming a superconducting dome. AFM ordering and the structural transition are fully suppressed near optimal doping. Further doping suppresses superconductivity and eventually terminates the dome. Figure is from Ref [22], reporting T_s from X-ray data and T_c from magnetization data. T_N is from Ni *et al.* [20] and Fernandes *et al.* [21].

being a rational, symmetrical intergrowth of two or more individual crystals of the same species [24]. That is to say two separate crystals, which share lattice points, for different rotations of the same crystallographic structure.

There are three main causes of types of twin formation: *growth twins, gliding twins, and transformation twins.*

As the name suggests, growth twins form during crystal growth and occurs either as a result of the intergrowth from multiple nucleation points or from environmental factors. This often results in large twin domains such as those in the twinned pyrite crystal in Fig 1.1.

Glide twins occur as a result of a crystal plastically yielding to stress causing the

translation of large sections of crystal planes. In some cases the glide twins remain after the stress is removed if there are local minimums in the structural energy and there are large barriers separating them from the lowest energy state. *Shocked quartz* is a notable example, which is only found at the site of meteor impacts and nuclear detonations.

Transformation twins, result from a crystal undergoing a symmetry lowering which usually takes place upon cooling. Transformation nuclei spontaneously appear in various parts of the crystal and grow domains outward from their centers until reaching another domain or the edge of the crystal. In this fashion, the crystal is randomly populated with roughly equal populations of domains of each allowed orientation in the lower symmetry phase.

The iron-based superconductors do form growth twins. However the availability of large single crystals in the "122" family, allows for the selection of samples which are free of growth twins. For this reason the rest of the discussion will be limited to the transformation twins which arrise upon cooling through the tetragonal to orthorhomic transition in iron-based superconductors.

2.3.2 Domain Formation in Iron-based Superconductors

As noted above, upon cooling through T_N, the $A\mathrm{Fe_2As_2}$ crystals undergo a lowering of the crystal lattice symmetry from a tetragonal to orthorhombic symmetry driven by a sheer distortion. In the tetragonal phase, the a_T and b_T lattice vectors are equal in length (see Fig 2.5). In the orthorhombic phase the a_O lattice vector is longer than the b_O by as much as a_O/b_O=1.013 in the parent compound, $\mathrm{CaFe_2As_2}$.

This distortion can occur in four different directions and in a free standing crystal each possible direction for distortion is equally likely. Upon cooling through T_N, this distortion beings at multiple nucleation points and begins growing domains in long thin strips until reaching the edge of the sample or another domain. Thus the sample becomes equally populated with a random distrobution of the four allowed twin domains

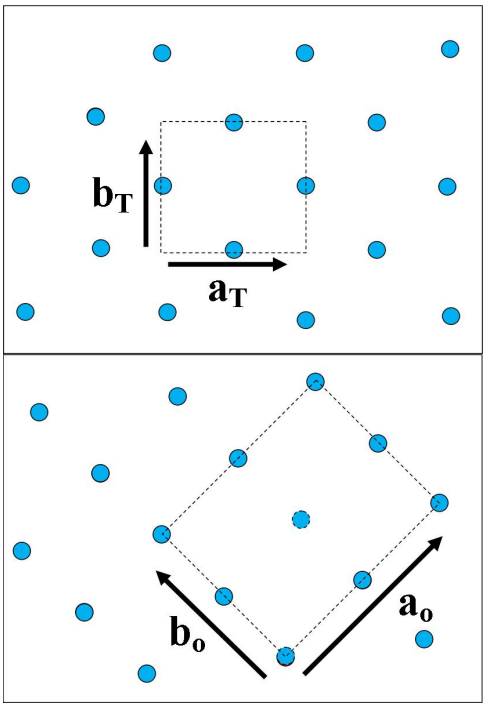

Figure 2.5 Top panel: At ambient conditions the $A122$ compounds have a tegragonal crystal symmetry (pictured in 3D in Fig 2.1). In this configuration the a_T and b_T lattice vectors are of equal length. Bottom panel: upon cooling through T_N (see Table 2.1), the crystal symmetry is lowered to an orthorhombic symmetry.

as is schematically represented in the right panel of Fig. 2.6. As noted above, these twin domains are crystallographically identical, but with different rotations of their orthorhombic axes.

As the sample is equally populated with the four different domain orientation, measurements of anisotropy within the ab-plane become impossible for any bulk measurement. For example if one wants to make a resistivity measurement, an equal fraction of the the electrical current with flow through domains whose a_O-axis is parallel to the current as those domains whose b_O-axis is parallel to it.

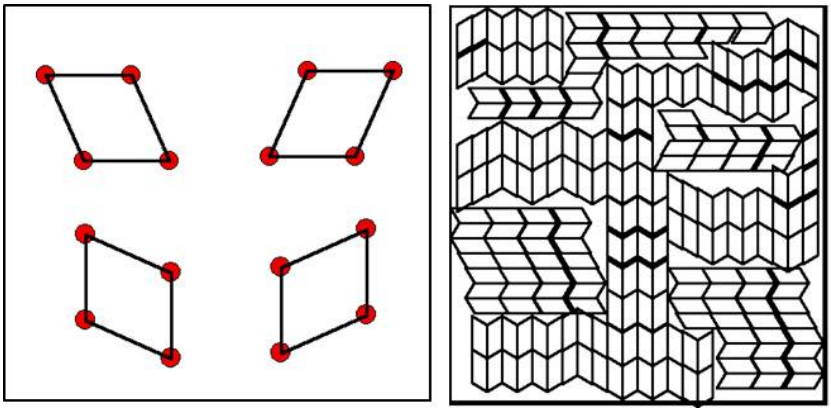

Figure 2.6 Left Panel: Orthorhomic distortion of the lattice occurs in four different allowed orientations. Right Panel: Schematic representation of a free standing sample after becomeing equally populated with domains of each of the four allowed orientations of the distortion after cooling through the structural phase transition.

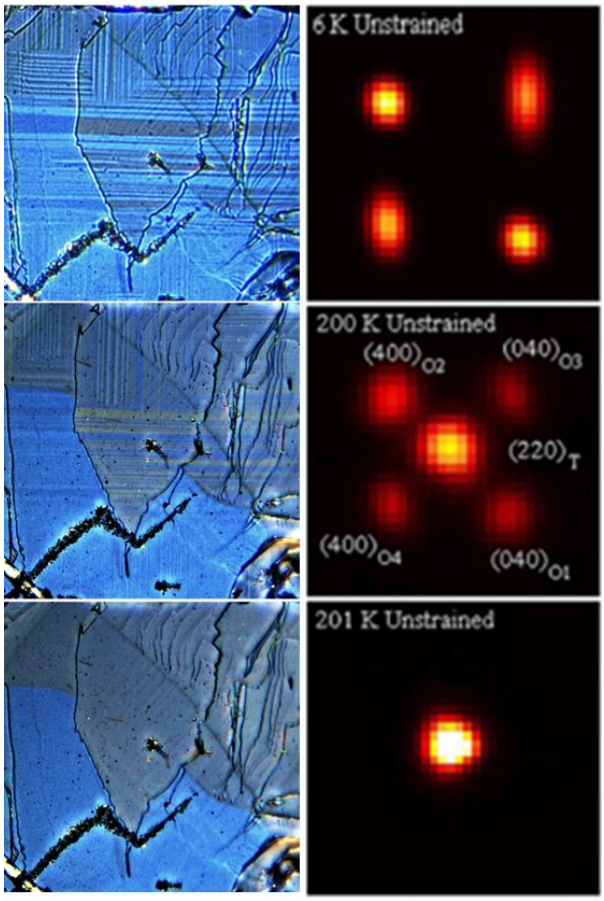

Figure 2.7 A comparison of domain evolution with temperature as viewed by polarized optical microscopy (left panels) and X-ray diffraction (right panels) in $SrFe_2As_2$ (for experimental details see Chapter 3). The top panels show data taken at 6 K, deep in the Ort/AFM state. The long thin stripes in the polarized microscopy images show the presence of twin domains. Four peaks can be seen in the X-ray diffraction pattern corresponding to the four orthorhombic domain orientations. The center panels show the same sample at 200 K. Domains are much fainter than in the top panel as the intensity is proportional to the orthorhombic distortion (see 3.2.1). At this temperature the four orthorhombic twin domain peaks are also visible as well as the tetragonal peak, clearly showing the coexistence of the tetragonal and orthorhombic phases. Bottom panels: At 201 K the sample is entirely in the tetragonal phase and magnetically unordered. As there are no longer twin domains, no stripes can be seen. Similarly only a single peak corresponding to the tetragonal symmetry remains.

CHAPTER 3. Experimental Methods and Analysis

This chapter begins with the details of preparing samples for experimental measurements. The research presented here requires large, plate-like, single crystal samples in order to probe in-plane anisotropy. This process begins by growing the crystals. Samples must then be cut into strips of proper dimensions along specific directions with respect to the crystallographic structure. This chapter then goes on to describe the experimental techniques and equipment used in this work.

3.1 Sample Growth and Preparation

3.1.1 Crystal Growth

AFe_2As_2 crystals studied in this work were grown using either FeAs or Sn flux. This process includes firing elemental components to create polycrystalline material which is then mixed with a flux, sintered again, and slowly cooled to produce large crystals, after which the flux may be decanted away from the crystals. A typical example growth for $SrFe_2As_2$ follows:

> *"Elemental Sr, Fe, and As were fired at 850 C for 12 h and 900 C for 20 h with intermediate grinding. The prefired pellet, which contains mainly SrFe2As2 with 5% FeAs impurity, was broken into smaller pieces and added to Sn flux in the ratio of SrFe2As2 : Sn=1:48 and placed in a 2 ml crucible. A catch crucible containing quartz wool was mounted on top of growth crucible and both were sealed in a silica ampoule under approximately 1/3 atmosphere of argon gas. The packing and assembly of the growth ampoule were performed in air since the prefired pellet is stable in air. The sealed ampoule was heated to 1000 C and cooled over 36 h to 500*

> *C in a programmable furnace. At 500 C, the Sn was decanted from the SrFe2As2 crystals."* [Excerp from J.-Q. Yan, *et al.* (2008), Ref [18]]

Ideally plate-like crystals with dimensions up to 1 square cm by 1 mm thick can be grown by this technique. However, typical crystals studied here, had dimensions of 3-4 mm across and 0.5 mm thick.

3.1.2 Preparing Samples

The majority of this work focuses on anisotropy between the orthorhombic crystallographic $\mathbf{a_o}$ and $\mathbf{b_o}$ directions which requires long narrow samples cut parallel the orthorhombic directions. The orthorhombic crystallographic directions lie at 45 degrees to the tetragonal axes. As sample preparation was performed at room temperature (therefore in the tetragonal state) cleaving samples for anisotropy measurements was not possible as crystals cleave most readily along their crystallographic axes. This difficulty necessitated precise cutting parallel to the orthorhombic directions, rather than cleaving.

Samples were oriented using polarized optical imaging (described in detail in section 3.2.1). Samples were then glued to a glass substrate, using cyanoacrylate-based "super glue", and then cut on a precision wire saw. Cuts are made using an oscillating 50 um wire blade with a continuous abrasive slurry drip. The abrasive slurry consists of 300 mesh carborundum powder suspended in glycerin. This allows for cuts with a notch width of about 60 um and easily allows cutting samples with a minimum dimension of 0.5 mm. The cyanoacrylate glue can easily be dissolved with acetone to remove the sample from the glass substrate.

Contact leads for both straining and resistivity measurements, described in 3.2.3 and 3.3, were made by soldering thin silver wires with tin based solder (U.S. Patent 8,450,246, Ref [25]) Initial experiments were performed using 125 μm diameter wires. Futher experimentation showed that 50 μm were more suitable, as they are much less rigid and therefore create less unintended strain in samples. Samples were glued to either

a hypodermic needle or a glass substrate to stabilize them during soldering. This was usually done with silver paste which can easily be dissolved.

Figure 3.1 A typical sample mounted on the end of a hypodermic needle. Contact leads have been soldered to the sample in a four probe resistivity configuration. A penny in the background gives the reader an impression of the size of a sample.

3.2 Experimental Techniques

3.2.1 Polarized Microscopy

Domains in iron-based superconductors exhibit the optical properties of birefringence and dichroism. The property of birefringence causes the index of refraction to change depending on the direction of the polarization vector of light incident on the sample. Dichroism, on the other hand, is a property where a materials absorbtion spectrum varies with polarization direction. In iron-based superconductors, the directional dependence of

these optical properties depends on the polarization direction relative to the orientation of the domains. These properties can be exploited to allow for direct visualization of domains under polarized microscopy [26].

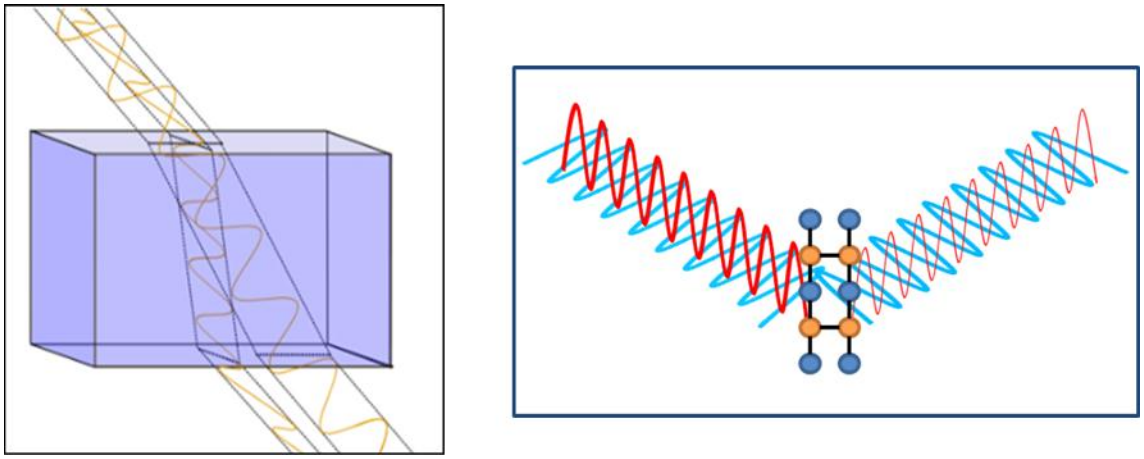

Figure 3.2 Domains in iron-based superconductors exhibit the optical properties of birefringence and dichroism. Left panel: In birefringence, the index of refraction changes depending on the direction of the polarization of light passing through it. Right panel: In dirchroic materials, the absorbtion spectra changes depending on the direction of the incident light's polarization direction.

This work utilized a Leica DMLM polarized microscope. White light is directed through a polarizer and shined onto a sample. The reflected light then passes through the microscope objective, followed by an analyzer and onto a CCD camera. The polarizer and analyzer are nearly in the crossed position. This configuration allows one to see a contrast between the domains due to the birefringence and dichroic properties discussed above.

The microscope is set atop a continious flow liquid helium coldfinger inside an evacuated cryostat. Samples are mounted to the cold finger using thermal grease. This configuration allows for temperatures in the range of 5 K to 300 K.

When imaging domains, the highest contrast is observed when the sample is aligned with the [100] tetragonal direction at a 45^o to the polarization direction of incident light (parallel and perpendicular to the orthorhombic a_o in different domains.) The contrast of

domain images depends on the quality of the surface and the homogeneity of the samples. The color of the domains depends on the orientation of the orthorhombic directions with respect to the polarizer and is not a consequence of sample's chemical composition.

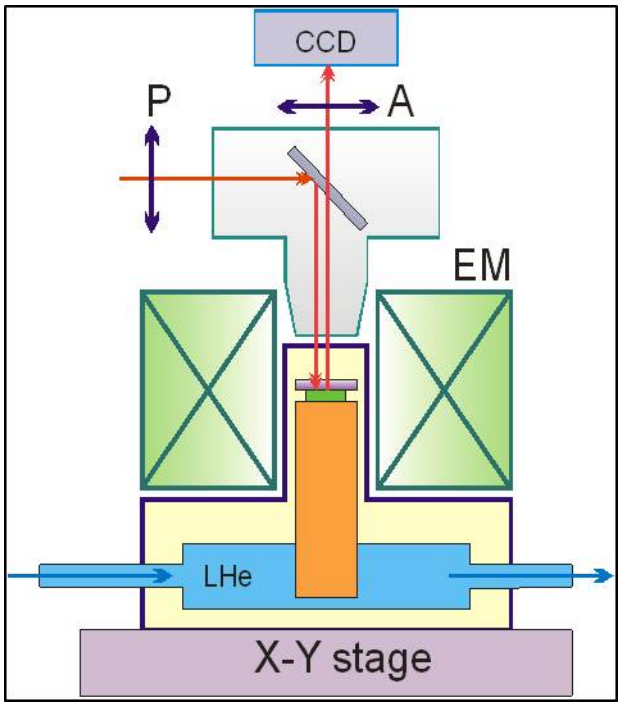

Figure 3.3 A schematic diagram of the polarized microscope used in this work. Incoming white light is polarized and reflected off a splitter. The light then reflects off the sample surface and passes back up through the splitter and then through an analyzer. Finally the image is recorded by a CCD camera.

3.2.2 X-ray Diffraction

X-ray measurements presented in this work were performed in the MUCAT sector (beamline 6ID-D) of the Advanced Photon Source, at Argonne National Lab. The experiments were performed at 99.3 keV giving an absorbtion length of the X-rays of about 1.5 mm. This allows full penetration through typically 0.05 to 0.1 mm thick samples, mounted with their **c** direction parallel to the incident x-ray beam. The beam size is reduced to 0.2x0.2 mm^2 by a slit system. As a result, each measurement averages over the entire sample *volume* selected by the beam dimension in the (**ab**) plane and its pro-

jection through the sample along the **c** direction. The direct beam was blocked by a beam stop behind the sample. Two-dimensional scattering patterns are measured by a MAR345 image-plate positioned 1730 mm behind the sample. During the recording, the sample is tilted through two independent angles, μ and η, perpendicular to the incident x-ray beam by 3.2 deg. Typical exposures were 10 minutes each.

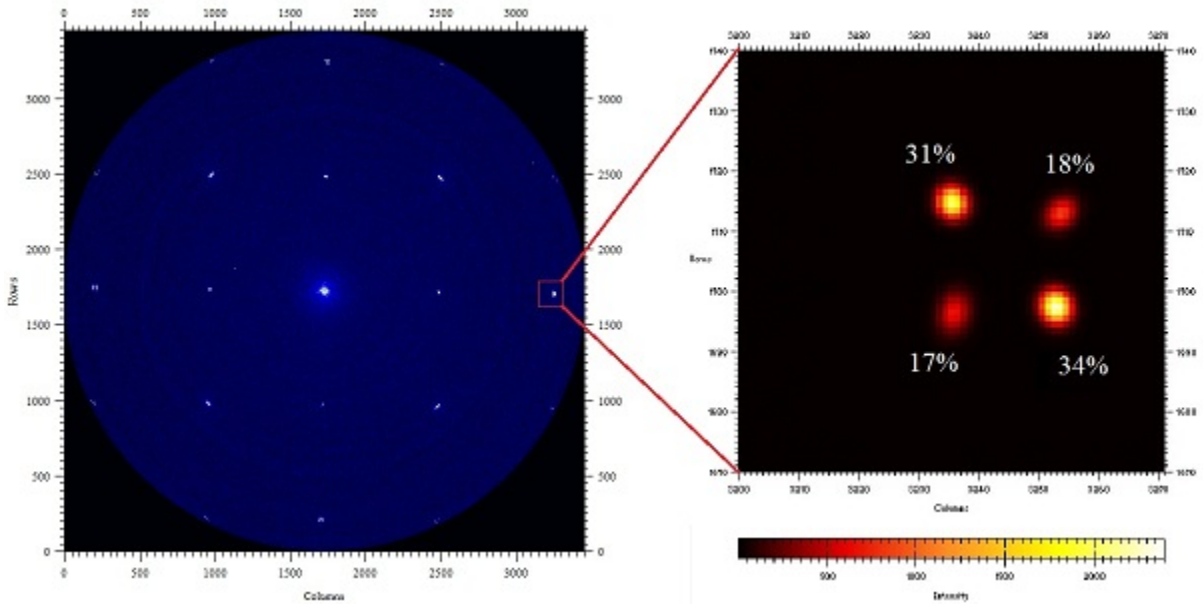

Figure 3.4 Visual representation of X-ray diffraction data. The left panel shows one complete X-ray exposure. The bright spots are Bragg peaks. The right panel shows a zoom on one of the Bragg peaks in the left figure. The original Bragg peak is actually comprised of four split peaks corresponding to each of the four twin domain orientations. The relative intensity of each of the split peaks is proportionate to the total volume fraction of the corresponding twin domain orientation within the area probed by the beam.

The X-ray MAR data was analyzed using the program, Fit2D. Data is stored as an array of 3450x3450 pixels. Each pixel tallies the total number of x-ray counts at that pixel site, during the length of the exposure. Individual Bragg peaks are fit to a two dimensional gaussian to determine the peak centers and to allow for integration of the total number of X-ray counts within a peak.

3.2.3 Resistivity Measurements

Temperature dependent resistivity measurements were performed in a *Quantum Design* Physical Property Measurement System (PPMS). The bulk of the resistivity measurements in this work were made in the range of 5 K to 300 K. Typically warming and cooling rates were set at 5 K/min with data points collected every 0.25 K. In the vicinity of the structural and magnetic phase transitions, many compositions show a dramatic temperature dependent evolution of the resistivity necessitating more careful measurements and a larger density of data points. For this reason the warming and cooling rates were slowed to 1 K/min with data points collected every 0.1 K for a window of roughly 25 K above and below the structural and magnetic transitions. All measurements were performed using the standard four-probe method.

3.3 Detwinning

3.3.1 Uniaxial Force Detwinning

As discussed above, iron-based superconductors and their parent compounds undergo a structural transition from a tetragonal to orthorhombic symmetry upon cooling through T_s. As this happens the sample divides into many twin domains comprised of four different rotations of the orthorhombic ab-plane. This makes any bulk measurement of anisotropy impossible, thus necessitating a technique to detwin the sample.

3.3.2 The Horseshoe Straining Device

The underlying principle of detwinning via uniaxial force is quite simple: When a strain is applied through a sample, the most energetically favorable orientation is when the longer axis, a_o is parallel the direction of the strain. Similarly if a stress is apllied through a sample, it becomes most favorable for the shorter axis, b_o, to be parallel to

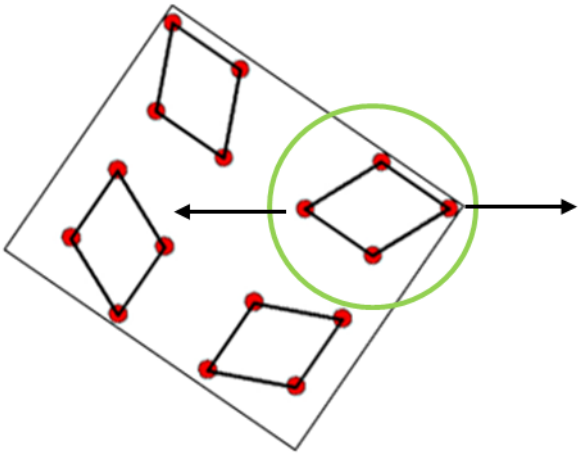

Figure 3.5 In the twinned state, samples are separated into many twin domains. When a strain is applied to a sample, the most energetically favorable orientation is one with the longer orthorhombic axis, a_o, along the direction of the strain.

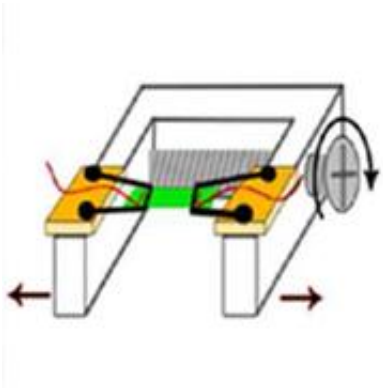

Figure 3.6 Schematic drawing of the horseshoe deviced for straining samples.

the direction of the stress. The degree of energetic favorability naturally depends on the magnitude of the force.

For this work, a straining device was designed, consisting of a "U"-shaped brass frame, which can be deformed by a mechanical push screw, causing the frame to open up. This device is nicknamed a "horseshoe" and will be refered to as such throughout the rest of the text. Silver wires, ranging from 50-125 μm are soldered to the ends of the samples and then soldered to the ends of the horseshoe. By this means, as the horeshoe is deformed, the contact wires tighten and strain the sample. These straining contact

wires also act as voltage leads for a standard four probe measurement described in the section on resistivity (3.2.3).

The horseshoe can also be used to stress a sample. In this case the pushscrew is tightened prior to mounting a sample on it and so the horseshoe is open during mounting. After the sample is mounted on the horseshoe, the pushscrew may then be loosened causing the horseshoe to close and apply a stress on the sample. For this process 125 μm contacts are necessary as thinner contacts simply bend as the horseshoe closes. This work focused on strain detwinning, but all the descriptions can also apply to stress detwinning.

3.3.3 Completeness of Detwinning

It is difficult to determine the magnitude of the strain produced by the horseshoe and therefore to precisely apply the necessesary force to detwin a sample. For this reason the easiest method is to incrementally increase the strain and examine the relative domain population. The most direct way to do this is using X-ray diffraction (technical description above). Limitations on the availability of access to high energy X-ray facilities and time make it infeasible to do diffraction measurements on every sample.

Polarized optical microscopy provides an efficient way to determine if sufficient strain has been applied to detwin a sample, but lacks the accuracy of X-ray diffraction. For this reason, samples were incrementally strained and imaged under polarized microscopy after each strain increment, until domains were no longer visible. X-ray diffraction was then performed on these samples and the results demonstrated that when domains are no longer visible under polarized microscopy, approximately 90% of the sample volume is represented by the dominant domain orientation (i.e. the one whose orthorhombic a_o axis is parallel to the strain).

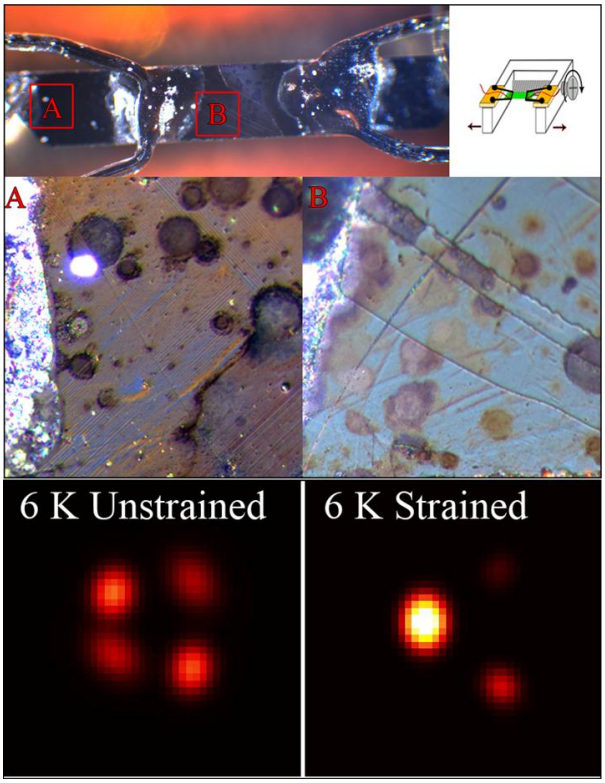

Figure 3.7 X-ray data of $BaFe_2As_2$ corroborates that polarized microscopy can be used to determine if samples are detwinned. The top panel shows a sample mounted on a horseshoe. Immediately below that are polarized microscopy images of both the unstrained/twinned region (label A, left) and the strain-detwinned region (label B, right). The bottom panel shows the corresponding X-ray data, centered on the position of the (400) orthogonal Bragg peak. The unstrained region (left) shows four roughly equal intensity Bragg peaks corresponding to each of the four domain orientations, and demonstrating they represent nearly equal parts of the sample volume fraction. In the strained region (right), a single peak comprises about 90% of the total intensity, suggesting that the dominant domain occupies roughly 90% of the volume fraction. This data and similar measurements on $SrFe_2As_2$ demonstrate that polarized microscopy is an effective way to determine if a sample is nearly detwinned.

CHAPTER 4. Detwinning and Resistivity Anisotropy in $SrFe_2As_2$

4.1 Summary of Results for $SrFe_2As_2$

Intrinsic, in-plane anisotropy of electrical resistivity was studied on mechanically detwinned single crystals of $SrFe_2As_2$ above and below the temperature of the coupled structural/magnetic transition, T_s. Resistivity is smaller for electrical current flow along the orthorhombic a_o direction (direction of antiferromagnetically alternating magnetic moments) and is larger for transport along the b_o direction (direction of ferromagnetic chains), which is similar to $CaFe_2As_2$ and $BaFe_2As_2$ compounds. A strongly first order structural transition in $SrFe_2As_2$ was confirmed by high-energy x-ray measurements, with the transition temperature, and character unaffected by moderate strain. For small strain levels, which are just sufficient to detwin the sample, there is a negligible effect on the resistivity above T_s. With the increase of strain, the resistivity anisotropy starts to develop above T_s, clearly showing the relation of anisotropy to an anomalously strong response to strain. This study suggests that electronic nematicity cannot be observed in the FeAs based compounds in which the structural transition is strongly first order.

4.2 Experimental

Single crystals of $SrFe_2As_2$ were grown out of tin flux and were characterized by single crystal x-ray diffraction [18]. Resistivity measurements were also reproduced on FeAs flux grown [13] showing a similar transition temperature to Sn-grown samples. The crystals

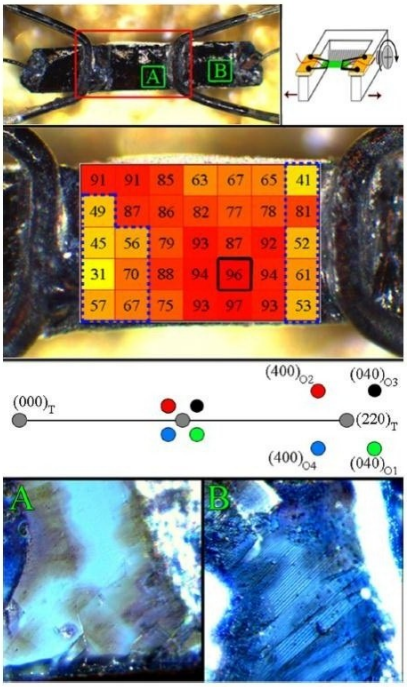

Figure 4.1 Top panel- a schematic of the sample mounted on a "horseshoe".. The second panel shows a zoom of the central area of a $SrFe_2As_2$ sample, overlaid with a spatial map, taken at 6 K, of the percentage of domain population with orthorhombic distortion along the strain (domains O2, O4 in the schematic presentation of the x-ray Laue pattern, third panel) as determined from the integrated x-ray intensity over all four possible domains, with actual x-ray data shown below in Fig. 4.2. Thick dashed lines at potential contacts show the area above the soldered contact. The bottom panel shows polarized optical microscopy images, of the same sample, in the strained (left) and unstrained (right) areas at 5 K, revealing mechanical detwinning on the surface of the sample between potential contacts.

were cut into strips along the tetragonal [110] $_T$ direction (which below $T_{\rm TO}$ becomes either the $[100]_o$ a-axis or $[010]_o$ b-axis in the orthorhombic phase.) Mechanical strain was applied through either thick (0.125 mm) or thin (0.05 mm) silver wires, soldered to form voltage probes [27], see top panel in Fig. 4.1. The ends of the wires were mounted on two insulator boards attached to a brass horseshoe. The horseshoe was deformed by a stainless push-screw, and thereby strained the crystals. Thin silver wires (0.050 mm) were soldered to the ends of the samples to form current leads. These wires were bent so as to create minimal strain. Use of thinner wires for transmission of strain resulted

in improved control of strain in the samples. Four-probe resistance measurements were carried out in a *Quantum Design PPMS* from 5 K to 300 K. Visualization of structural domains in unstrained samples and their absence in detwinned samples was performed in a ^{4}He flow-type cryostat mounted on the table of a polarized - light *Leica DMLM* microscope (see section 4.2.1). Samples were imaged before and after the application of strain from room temperature to 5 K. The highest contrast of images was achieved for a configuration when the tetragonal [100] direction was 45^o with respect to the polarization plane. High-energy x-ray measurements were performed on detwinned $SrFe_2As_2$ grown out of Sn-flux selected by the criterion of the sharpness of their resistive features and polarized optical imagaig. Measurements using high-energy x-rays were made from 6K to 215K in 10K increments through the entire temperature range and at 1K increments in the vicinity of the structural transition.

4.3 Results

4.3.1 Detwinning

To obtain twin-free regions in the samples, crystals were strained at room temperature and kept under strain while measuring temperature-dependent resistivity and studying domain images with polarized light microscopy at 5 K. Strain was progressively increased until no twins were observed in the area between potential contacts. The images in the bottom panels of Fig. 4.1 illustrate the effect of the strain in detwinning $SrFe_2As_2$, with a zoom of the spots on the sample (as shown in the top panel) in the strained (left) and unstrained (right) areas. The entire area of the crystal between the straining contacts ($\sim 1.8 \times 0.6$ mm^2) was found to be essentially free of twins under polarized microscopy.

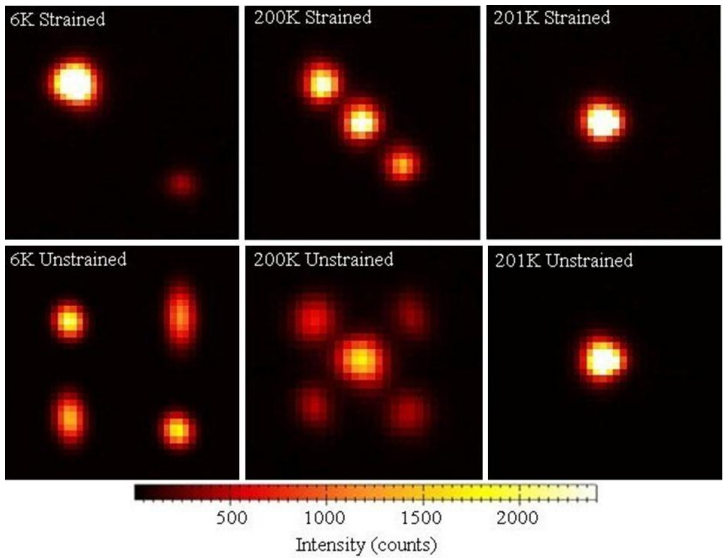

Figure 4.2 $SrFe_2As_2$ temperature evolution of the $(220)_T$ peak of high energy x-ray Laue patterns in twinned and detwinned parts of the crystal, as shown in Fig. 4.1. At 6 K, four peaks in the twinned part of the crystal correspond to four twin domain orientations, with very close to equal populations ranging between 23 and 26% of the sampled volume. In the strained portion of the crystal, the dominant spot comprises ∼96% of the integrated peak intensity, the second spot approximately 4%, while the other two peaks go below our resolution limit (∼ 0.1%). Phase coexistence of the orthorhombic and tetragonal peaks at 200 K (second panel) clearly illustrates that (1) the structural transition remains at the same temperature and is first order; (2) the domain population clearly changes with temperature. The phase coexistence disappears abruptly within a 1 K step, as seen in both the strained and unstrained regions of the sample (right panels) in 201 K image, where the orthorhombic peaks are completely gone.

4.3.2 X-ray

Scanning the x-ray beam across the sample allows a spatially resolved characterization of the domain population as demonstrated in the second panel of Fig. 4.1. The map shows spatial distribution of the percent volume fraction of the crystallographic domains with distortion along the strain in the crystal. This was obtained by the analysis of the x-ray intensity distribution in the 6 K pattern arising from splitting $(220)_T$ peak, as schematically shown in the third panel in Fig. 4.1. In the twinned area of the crystal, four possible crystallographic domains, with orientations along a_o (O2 and O4) and b_o

(O1 and O3) are equally populated, leading to four equal intensity spots. Application of strain makes formation of domains with the a_o axis along the strain energetically favorable, therefore in the strained regions, only two reflections are visible. The integrated intensities of these two reflections reveal relative orthorhombic domain populations of about 96% and 4 % for the two visible reflections.

As can be seen from the map, areas under the soldered contacts show random domain populations. In the strained part of the crystal between potential contacts, the volume fraction of a single domain reaches above 90%. Since we do not see any other domains in the polarized microscopy image, we come to the conclusion that the domain population may have depth profile. This would be naturally expected in our experiment, in which deformation is applied through the contacts soldered to one sample surface and can lead to depth profile in strain distribution. Despite the fact that detwinning is not complete in the bulk, we are able to get a clear trend in the temperature- dependent resistivity, since contact resistance is much smaller than sample resistance and thus contacts work to shorten the unstrained areas. As can be seen from the domain distribution map (second from top panel in Fig. 4.1), current flow between potential contacts (excluding the area of the contacts themselves, shown with dashed line) proceeds through the area in which 3 out of 24 pixels have a preferred domain population of 63 to 67%, 3 more pixels have a domain population of in 75 to 78% range, while the other 17 pixels have a volume population above 80% and block any direct current path between the contacts through the areas with low-percent domain population.

4.3.3 Resistivity

Resistivity measurements were performed using the same contacts on samples before and after application of strain. Nearly complete detwinning of the crystal, leads to a notable change of the temperature dependence of its resistivity. In Fig. 4.3 we show the resistivity of the same crystals #1 and #3 measured in the twinned and de-twinned

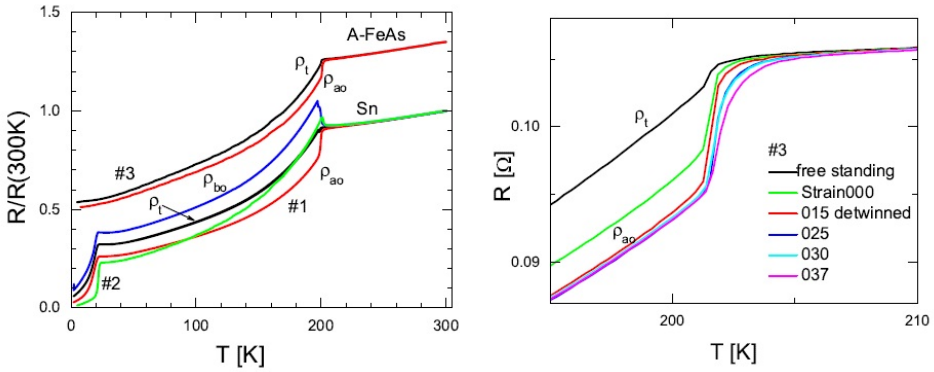

Figure 4.3 Left panel. Temperature dependence of resistivity, in $SrFe_2As_2$, measured along the tetragonal $[110]_T$ direction in twinned (ρ_t, black curves) and detwinned (ρ_{ao}, red curves) states for sample #1 grown from Sn flux and sample #3 grown from FeAs flux with subsequent annealing (A-FeAs). The blue line shows the calculated temperature-dependent resistivity for #1 in the ρ_{bo} direction. The green line shows the temperature-dependent resistivity for another Sn-grown sample #2, partially detwinned by application of stress with a preferable orientation of domains in the b orthorhombic direction. The right panel shows the temperature dependent resistivity for sample #3 in the vicinity of the structural transition as a function of relative strain (in arbitrary but monotonically increasing units). The red curve (015) shows the resistivity in the detwinned state, showing a sharp transition with no features above T_{TO}. With further increase of strain the feature at the transition broadens and reveals strain-induced resistivity anisotropy in the nominally tetragonal phase.

states. The partial superconductivity in Sn-grown samples at 20 K is due to surface strain [28] associated with cleaving and shaping the sample and is not focus of this study. This trace superconductivity is not observed in the annealed samples. The resistivity, $\rho(T)$, of unstrained samples cut along the $[110]_T$ direction is very close to that measured on samples from the same batch with current along the $[100]_T$ direction [29]. It shows a feature at the structural/magnetic transition at ∼202 K. Straining the crystal gradually increases its resistivity at 300 K, however, the use of 0.05 mm diameter wires notably reduced fatigue, as compared with ∼1% value per strain as found in $CaFe_2As_2$ and $CaFe_2As_2$ compounds in our initial study [27].

Temperature dependent resistivity, measured with the current along the strain direc-

tion, $\rho_{ao}(T)$, shows a sharp drop (17% percent resistivity decrease in less than 1K change in # 1) immediately below the transition temperature T_{TO}, as opposed to a mild slope change in the twinned crystals. This sharp drop, as corroborated by imaging in polarized light, is the main resistive signature of the detwinned samples. Sharp jump-down is very similar to the behaviour found in strain-detwinned $BaFe_2As_2$ and $CaFe_2As_2$. This feature is not as pronouced in stress-detwinned samples [30], presumably due to incomplete detwinning in the direction perpendicular to the applied stress. Of note, the sharp feature at the transition remains at the same temperature, though the $\rho(T)$ dependence changes dramatically.

The resistivity of the sample #1, used in the x-ray study, reveals very weak anisotropy above the transition. To check if this anisotropy is associated with intrinsic anisotropy of the unstrained state (i.e. nematicity) or induced by the strain vector itself breaking rotational symmetry, we performed a systematic study of resistivity as a function of applied strain on yet another sample, #3. In the bottom panel of Fig. 4.3 we show temperature-dependent resistivity of the sample mechanically detwinned with systematically increasing strain. Strain values can be estimated to be in the 1 to 5 MPa range. As can be seen, the resistivity change above the transition, in the samples strained only enough to achieve a detwinned state (as found in polarized optical microscopy study), does not show any anisotropy above the transition. With further increasing strain, the resistivity changes its temperature dependence in the nominally tetragonal crystallographic phase and the transition is preceded by a range of decreased resistivity extending approximately 10 K above the transition. This observation suggests that small $\sim$1% anisotropy found in sample #1 above the transition is induced by strain vector.

4.3.4 Structural Order Parameter

To get further insight into the behavior of the structural order parameter, $\delta \equiv \frac{(a_o - b_o)}{(a_o + b_o)}$, we made a quantitative analysis of the temperature-dependent x-ray peaks (shown for

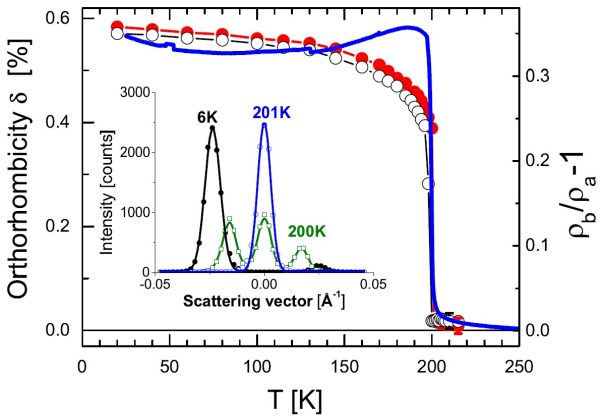

Figure 4.4 Temperature dependence of the structural order parameter $\delta = \frac{(a_o - b_o)}{(a_o + b_o)}$ as determined from the analysis of the $(220)_T$ spot splitting in single domain and twinned areas of the $SrFe_2As_2$ single crystal. The positions of the peaks were determined from the fit of the pixel profile to a Gaussian, as shown in the inset for strained area at three characteristic temperatures. Solid line shows anisotropy of electrical resistivity (right scale), normalized to match the magnitude of the structural order parameter at low and high temperature. Anisotropy peaks below the transition and finds a very small residual value above the transition, coinciding within error bars with the magnitude of the strained-induced lattice distortion.

selected temperatures in Fig. 4.2). The peak position was determined by fitting the intensity to a Gaussian shape, as shown in inset in Fig. 4.4.

The temperature dependence of the order parameter for the orthorhombic phase in strained and strain-free parts of the sample is shown in Fig. 4.4. The difference between the curves for strained and unstrained parts of the crystal as well as the tiny residual orthorhombicity above T_{TO} reflect the residual effect of strain. For comparison in Fig. 4.4 we show the calculated resistivity anisotropy of sample #1 in the orthorhombic plane, $\rho_{bo}/\rho_{ao} - 1$. The value of ρ_{ao} was measured directly in detwinned state of the sample. The value of ρ_{bo} was calculated from ρ_{ao} and resistivity measured in a twinned state of the sample, ρ_t, assuming random statistic averaging. As can be seen from comparison of the two quantities in Fig. 4.4, their relative changes above the transition are coinciding within error bars. Together with systematic evolution of resistivity in the tetragonal

phase as a function of strain, Fig. 4.3, this observation suggests that the tiny effect in resistivity above the transition comes from permanently applied strain.

4.4 Conclusions for Chapter 4

In conclusion, electrical resistivity of $SrFe_2As_2$ in the orthorhombic phase reveals unusual electronic anisotropy with a resistivity decrease along the a-axis (direction of antiferromagnetic spin ordering) and increase along the b-axis (ferromagnetic chain direction). This behavior and temperature dependence of the anisotropy, $\rho_{bo}(T)/\rho_{ao}(T)$, with a maximum at/or slightly below T_{TO}, is similar in all parent AFe_2As_2 compounds. The magnitude of the anisotropy monotonically increases with the ionic radius of the alkaline earth element, A. The resistivity anisotropy in $SrFe_2As_2$ is negligible above the strongly first order structural transition. However, the anisotropy in the tetragonal phase is easily induced by the application of a mild strain in the MPa range, suggesting a strong responsiveness of the compound. Our results suggest that electronic nematicity may not be observed in materials with a strong first order character of the structural transition. Additional studies are needed to clarify the effect of the strain itself on the electronic anisotropy in $BaFe_2As_2$ based materials to study the origins of the experimentally observed electronic anisotropy (nematicity) above the structural transition.

CHAPTER 5. Resistivity Anisotropy and Effect of Strain in $BaFe_2As_2$

5.1 Summary of Results from $BaFe_2As_2$

In this section, the effect of uniaxial mechanical strain on the structural/magnetic transition in the parent compound of the iron arsenide superconductor, $BaFe_2As_2$, is characterized by temperature-dependent electrical resistivity, x-ray diffraction and quantitative polarized light imaging. These measurements show that strain induces uniaxial structural distortion above the first-order magnetic transition and significantly smears the structural transition. This response is different from the ones found in the parent compounds, $SrFe_2As_2$ and $CaFe_2As_2$, in which coupled structural and magnetic transitions are strongly first order. This difference in the structural response explains the in-plain resistivity anisotropy above the transition in $BaFe_2As_2$. This conclusion is supported by the Ginzburg-Landau - type phenomenological model of the effect of the uniaxial strain on the resistivity anisotropy.

5.2 Experimental

Single crystals of $BaFe_2As_2$ were grown from an FeAs flux as described in Ref [20]. Crystals were cut into strips with typical dimensions of 0.6 mm wide, 3 to 5 mm long and had a thickness of approximately 0.1 mm. The lengthwise cuts were made parallel to the tetragonal [110] direction, which will become the orthorhombic $\mathbf{a_o}$ or $\mathbf{b_o}$ axes below the transition temperature (see 3.2.1 for cutting details).

Polarized light images were taken at temperatures down to 5 K using a *Leica DMLM* polarization microscope equipped with a flow-type ^{4}He cryostat. High-resolution images were recorded with a spatial resolution of about 1 μm. Measurements were done with the polarizer and analyzer nearly crossed.

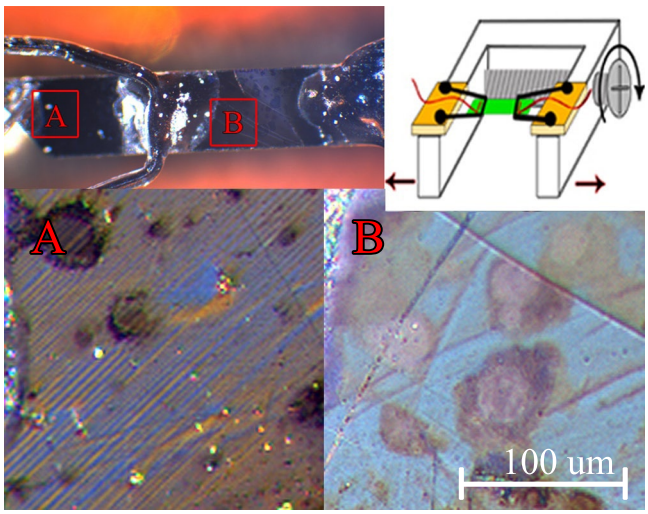

Figure 5.1 The top right panel shows a schematic of the horseshoe with the potential leads used to apply the strain by adjusting the push-screw. The current leads are mounted strain-free. The top left panel shows a $BaFe_2As_2$ sample, cut along the tetragonal [110] axis direction, with soldered contacts. The area "A" on the left side of the sample represents the unstrained region. Its polarized light image at 5 K (bottom left panel) reveals clear domain pattern by the alternating blue and orange stripes. The region "B" is located between the potential contacts in the strained part of the sample. It is shown in its detwinned state in the bottom right panel.

The leads for electrical resistivity measurements were formed by Ag wires, 50 μm in diameter, soldered to the samples with tin. Four-probe measurements were conducted in a *Quantum Design PPMS* from 5 K to 300 K. Measurements were first made on a free standing sample with the current leads mounted so as to produce no strain on the sample. Tensile strain was applied by means of a horeshoe straining device (see 3.2.3). The temperature-dependent resistivity was measured after every strain increment.

For the evaluation of the tensile stress value in our experiment we compared our data with the data of T. Liang (Ref. [31]), who found a roughly +5 K shift of the tetragonal-

to-orthorhombic transition feature upon a stress change from 15 to 50 MPa. Similar to Liang's data we observed an upward shift of about 3 K, which was achieved over four equivalent stress increments, which suggests that each strain increment is in the 4-5 MPa range for our horseshoe straining device. Therefore the strain at the highest level is estimated to be in the range of 16-20 MPa.

The sample was periodically imaged via polarized microscopy. The bottom panels in Fig. 5.1 show two areas of the sample: area A (left panel) is located between current and potential leads and remains twinned during measurements; area B (right panel) is located between the potential contacts in the strained part of the sample and becomes nearly twin-free under strain.

5.3 Results

5.3.1 Polarized Microscopy

The optical contrast of the domains is determined by the anisotropy of the bi-reflectance and is proportional to the orthorhombic distortion. It increases with decreasing temperature, and is weaker in $BaFe_2As_2$ than in $CaFe_2As_2$ [26]. Simultaneously, due to dispersion of the bi-reflectance, initially white incident light on reflection acquires color depending on the orientation of the orthorhombic axes with respect to the polarization direction of the incident light. This results in different colors of structural domains as can be seen in the bottom left panel of Fig. 5.1. Therefore, the color of the image contains information about the orthorhombic distortion, albeit in arbitrary units, and can be used for the analysis of its temperature dependence even in the detwinned state below the structural transition or in the strained state above the transition.

Figure 5.2 shows images from the strained region B of Fig. 5.1, below (130 K, left top panel) and above (160 K, left bottom) the transition. This region is completely detwinned by strain. The red square shows the small clean area of the sample, where

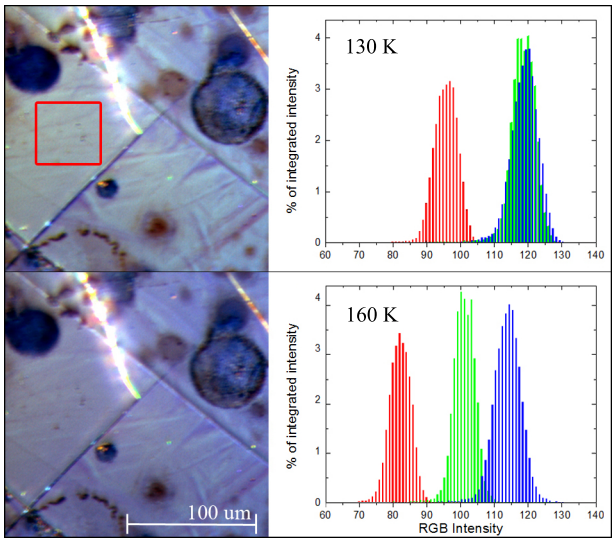

Figure 5.2 Left panels show polarized light images of the strained portion "B" of the sample below (130 K, top) and above (160 K, bottom) the structural transition temperature. The intensity in red, green and blue (RGB) channels for each pixel was digitized using 256 intensity bins. The total intensity was found by summing the intensities of all pixels in the selected region. The RGB color was characterized by the percent contribution of each channel to the total intensity, plotted against the value of each bin to produce the histograms. Right panels show the RGB histograms of a small area of the strained portion "B" of the sample, indicated by the red square in the top left panel at the same temperature. Whereas the blue channel remains almost unchanged, the intensities of the green and red channels shift dramatically indicating overall spectral change. The temperature dependence of this change is quantitatively analyzed in Fig. 5.3

the color of the image was analyzed numerically. The right panels in Fig. 5.2 show red-green-blue (RGB) histograms of that area. The images were taken every 5 K from 80 to 260 K in $BaFe_2As_2$. Fig. 5.3 shows the normalized intensity of the green channel, indicating that the structural distortion does not vanish abruptly at the transition but remains notable up to 200 K. For reference we show the results of the equivalent analysis in the parent compound $CaFe_2As_2$. Here the transition is strongly first order, and the data show no tail above the transition.

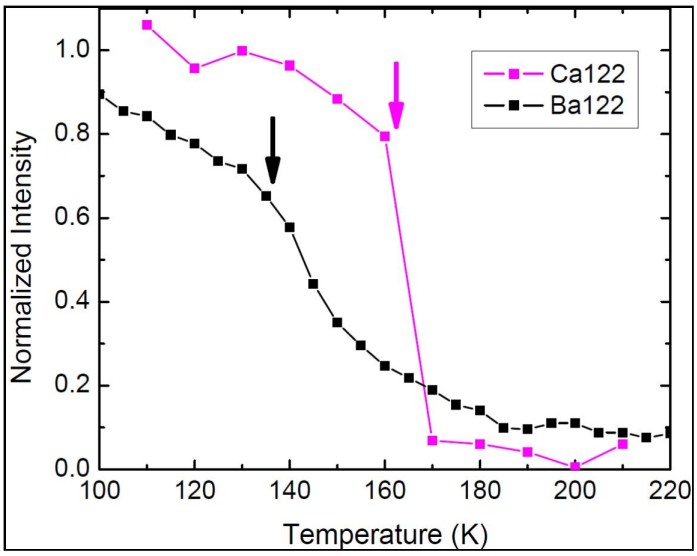

Figure 5.3 Normalized temperature variation of the green color channel's intensity through the magnetic transition in detwinned crystals of $BaFe_2As_2$ and $CaFe_2As_2$. Arrows indicate the temperatures of the respective magnetic transitions. While there is a clear signature of the transition at about 135 K in $BaFe_2As_2$, the curve changes smoothly through the transition with a second order character. In $CaFe_2As_2$, the transition is quite sharp around 160 K, and is strongly first order.

5.3.2 X-ray

X-ray analysis was done in both the unstrained (area A) and strained (area B) parts of the same crystal, as shown in Fig. 5.1. In the unstrained region, the tetragonal (220) Bragg peak splits below T_{TO} into four peaks, each representing a distinct orthorhombic domain, labeled O1, O2, O3 and O4. The four orthorhombic reflections merge back into a single tetragonal Bragg peak on warming above T_{TO} (see Fig. 5.4). The integrated intensities of the reflections at 6 K allow us to determine the relative population of orthorhombic domains. In the unstrained area, the population of the four domains ranges 19 to 31 % of the total peak intensity, characteristic of a near random distribution. In the strained region, the domain whose $\mathbf{a_O}$-axis lies along the direction of the strain accounts for nearly 90 % of the probed sample volume.

These effects are schematically described in Fig. 5.5. The separation between the

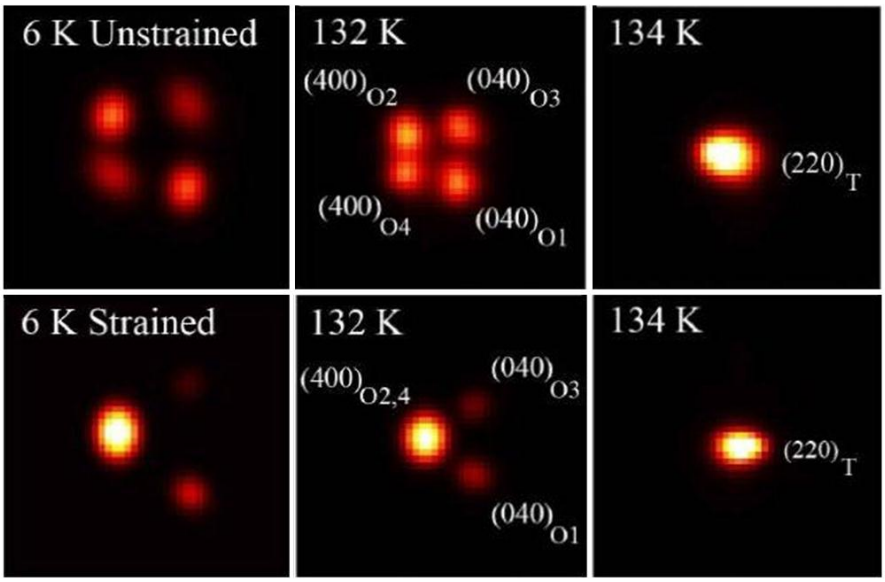

Figure 5.4 Temperature evolution of the two-dimensional x-ray diffraction pattern near the tetragonal (220) Bragg diffraction peak in $BaFe_2As_2$. Left and right columns of images show diffraction patterns in the unstrained and strained parts of the crystal, respectively. Four spots in the unstrained part at 6 K (top left) represent four domains in the sample with domain populations (proportional to integrated intensity) ranging between 19 and 31%, close to random). In the strained portion of the sample (6 K, top right panel), the dominant domain occupies nearly 90 percent of the volume of the sample area probed by the x-ray beam. Between 132 and 134 K, the sample undergoes an orthorhombic to tetragonal structural transition. The second-order nature of the transition is evidenced by the lack of coexistence of orthorhombic and tetragonal domains. This coexistence is clearly observed [32] in $SrFe_2As_2$ (see Fig. 4.2), in which the transition is strongly first-order, see Fig. 5.5 for schematic elaboration.

Bragg peaks resulting from the orthorhombic O1 and O2 domains is fixed because the relative angle between their twinning planes is fixed. The same is true for the peaks from the O3 and O4 domains. However there exists no such rule for the separation between the O2 and O4 peaks because the angle between their twinning planes is determined by their relative domain populations. In a sample with perfectly equal domain populations the four Bragg peaks would produce a square with each reflection having equal intensity. As the relative population of one domain orientation grows, the angle between the twinning

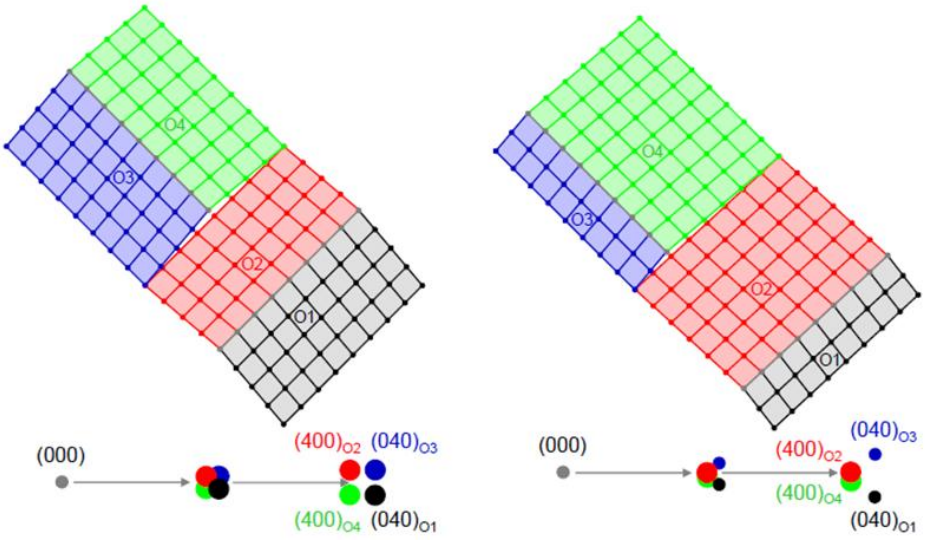

Figure 5.5 Schematic diagrams of the displacements of atoms in the twinned orthorhombic phase and the resulting Bragg reflections in $BaFe_2As_2$. As demonstrated in the top panel, a perfect crystal with equal populations of each domain orientation results in a square pattern between the (400) and (040) orthorhombic reflections. Conversely, the bottom panel illustrates the result of an unequal distribution of domain orientations. Here the angle between the O4 and the O2 domain orientations is significantly smaller and consequently moves the reflections closer together. Further, the population of each domain is proportional to the intensity of its Bragg reflection. These effects can be seen in the X-ray data of Fig. 5.4, especially the T=132 K panels.

planes of the O2 and O4 peaks becomes smaller and consequently the separation of the their Bragg peaks diminishes. This behavior is readily seen in the X-ray data in Fig. 5.4. The unstrained region of the crystal manifests relatively similar populations of each domain orientation and produces a pattern not quite square but slightly trapezoidal below the transition temperature. By contrast in the strained region of the crystal, where the dominant domain orientation represents nearly 90% of the sample volume, the O2 and O4 peaks are no longer distinguishable as two separate reflections.

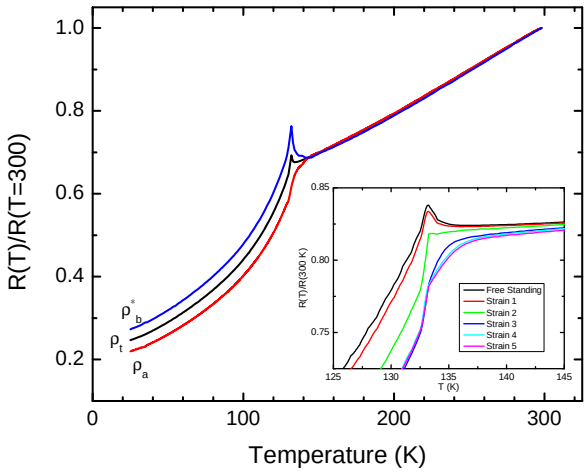

Figure 5.6 Temperature-dependent normalized resistivity, ρ_a(T)/ρ_a(300 K) of the $BaFe_2As_2$ sample in the free-standing, ρ_t (black curve), and strain-detwinned, ρ_a (red curve) regions of the same sample used for X-ray measurements in Figs 5.2, 5.3, and 5.4. The third (blue) curve shows ρ_b^*, calculated as $\rho_b^* = 2\rho_t - \rho_a$. The anisotropy can be seen for all temperatures below the transition, and a slight anisotropy can be found above the transition. Inset: Progression of the effect of increasing strain on the resistivity (ρ_a in the detwinned state). The black curve represents a free standing crystal. Tensile stress incrementally increases until reaching approximately 20 MPa for strain 5, see text for details. Strain 2 is sufficient to detwin the sample, revealing a sharp drop in resistivity at the transition. On further strain increase the jump rounds and its onset shifts up in temperature.

5.3.3 Resistivity

After sufficient stress was applied to detwin the crystals (the sample in Fig. 5.6 was nearly completely detwinned after the second strain increment, Strain 2, as determined by polarized optical imaging), we performed a careful study of the effect of additional stress on the resistivity anisotropy. As described the Experimental Methods section above, each strain increment represents a roughly 4-5 MPa increase in the stress from which we conclude Strain 2 to be in the 8-10 MPa range. The stress, whose magnitude at the highest level is estimated to be in the 20 MPa range, increases the onset temperature of the resistivity anisotropy. However the most dramatic effects of the resistivity change

are clearly around the point where the strain is sufficient to detwin the crystal.

5.4 Discussion

5.4.1 Strain Induced Anisotropy

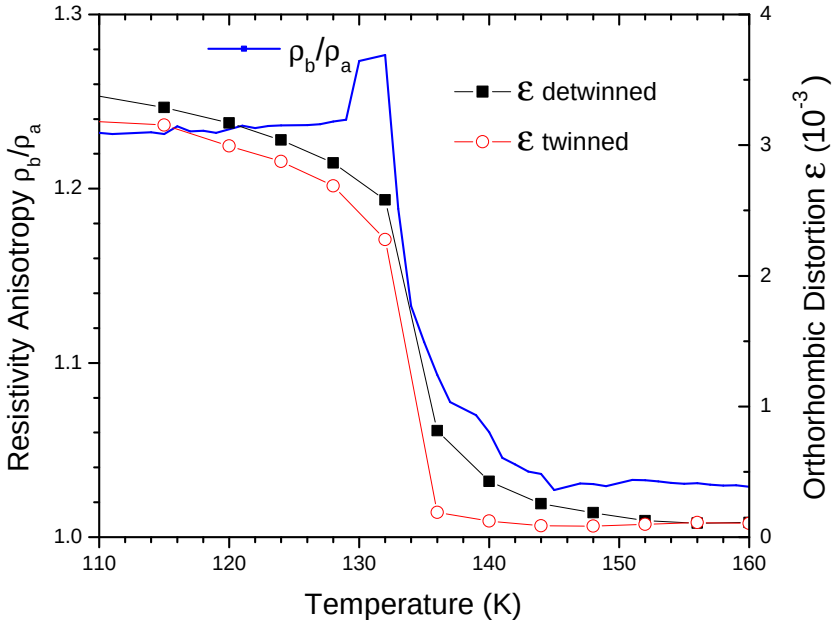

Figure 5.7 Comparison of the temperature-dependent resistivity anisotropy, $\frac{\rho_b^*}{\rho_a}$, and the orthorhombic distortion, $\epsilon = \frac{(a_O - b_O)}{(a_O + b_O)}$ in the temperature range close to T_N, in $BaFe_2As_2$. Both quantities show a pronounced "tail" above a sharp drop in the order parameter at 135 K, revealing that the anisotropy is directly related to strain.

Figure 5.7 shows a direct comparison of the temperature-dependent degree of the orthorhombic distortion, $\epsilon(T)$, and of the resistivity anisotropy, ρ_b/ρ_a, in the same sample of $BaFe_2As_2$ under identical strain conditions. The two quantities reveal a clear correlation. Both show a rapid rise below approximately 135 K with decreasing temperature. In addition both ϵ and ρ_b/ρ_a show a clear "tail" above 135 K, in agreement with the color analysis discussed above. In strain-free samples of $BaFe_2As_2$, the tetragonal-to-orthorhombic structural transition at T_N is of the second order and precedes a strongly first-order magnetic transition at $T_N \leq T_{TO}$ [33]. It is then natural to assign the rapid

increase of the anisotropy below 135 K to a magnetic transition, while the "tail" above 135 K correlates with the orthorhombic distortion. The exact meaning of the structural transition in the presence of the strain field becomes unclear, as the order parameter varies smoothly with temperature. Therefore from this direct comparison we conclude that externally applied strain is the cause of the structural and transport anisotropy above T_{TO}.

5.4.2 Comparison of the effect of strain on first and second order transition: $BaFe_2As_2$ vs $SrFe_2As_2$

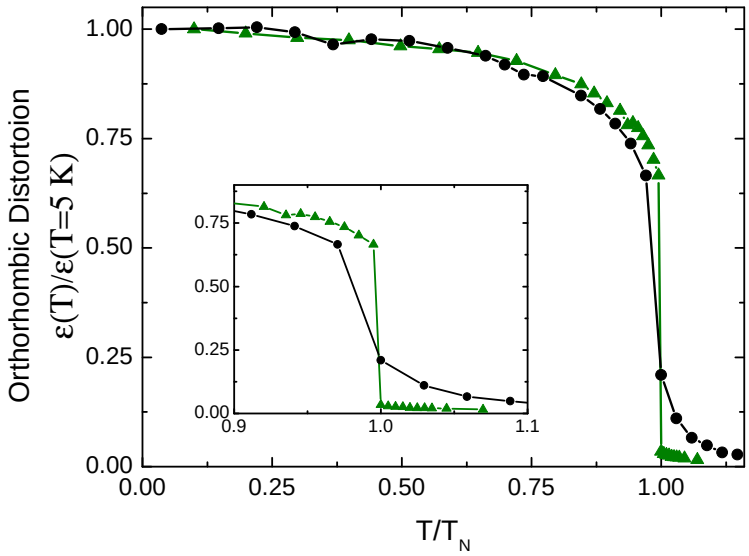

Figure 5.8 Comparison of the temperature-dependent orthorhombic distortions, $\epsilon = \frac{a_O - b_O}{a_O + b_O}$, in strain detwinned areas of $SrFe_2As_2$ (green triangles), Ref.(detwinning2), and $BaFe_2As_2$ (black circles). The data are presented vs. normalized temperature T/T_N. A pronounced "tail" above T_N in $BaFe_2As_2$ is caused by an anomalously strong susceptibility of the lattice to strain.

In Fig. 5.8 we compare the temperature dependent orthorhombic distortions, ϵ, for two strained AFe_2As_2 compounds each with a very different character of the transition: strongly first-order in $SrFe_2As_2$ and second order in $BaFe_2As_2$. The data are plotted on

a normalized temperature scale, T/T_N. As is clear from the Figure 5.8, the "tail" of the anisotropy above the transition is virtually absent in $SrFe_2As_2$, whereas it is quite noticeable in $BaFe_2As_2$.

5.5 Phenomenological model of the effect of uniaxial strain

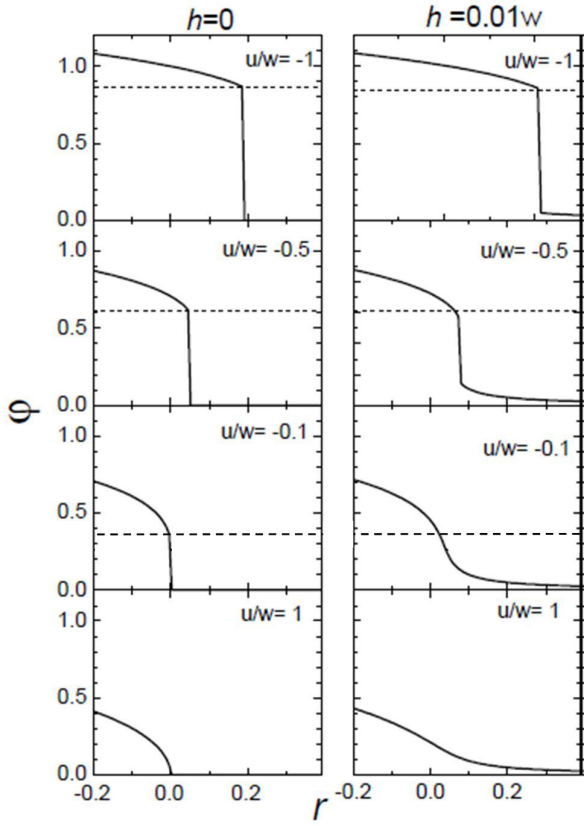

Figure 5.9 Evolution of the anisotropy parameter $\varphi \propto \rho_b - \rho_a$ vs. temperature parameter r, $r \propto T - T_s^0$. Left column of panels is for $h = 0$, right column is for $h = 0.01w$. The bottom pair of panels shows a second-order transition for u=w=1, the other pairs of the panels show first-order transitions for u=-w, u=-0.5w and u=-0.1w (top to bottom). The dashed lines show the size of the jump $\Delta\varphi$ in the absence of an external field.

Regardless of which electronic degree of freedom φ is responsible for the electronic anisotropy, it should be proportional to the orthorhombic distortion, since both break the tetragonal symmetry of the lattice close to T_{TO}. For example, φ can be associated

with magnetic fluctuations [41]. By symmetry, ϕ and ϵ are bilinearly coupled in the free energy expansion, i.e. they give rise to the term $\phi\epsilon$. Since the external strain σ also couples bilinearly to the orthorhombic distortion $\epsilon = (a_O - b_O)/(a_O + b_O)$, it has an effect on ϕ similar to that of a magnetic field h on Ising ferromagnets. In order to compare the effect of a finite h on the second-order and the first-order structural phase transitions, we consider the phenomenological free energy:

$$F = \frac{r}{2}\varphi^2 + \frac{u}{4}\varphi^4 + \frac{w}{6}\varphi^6 - h\,\varphi \tag{5.1}$$

with temperature parameter $r \propto T - T_s^0$, where T_s^0 is the mean-field structural transition temperature. Here u and w are phenomenological parameters of Ginzburg-Landau theory describing the phase transition. (Note that a similar Ginzburg-Landau approach was employed by A. Cano [44]) to address the order of the magneto-structural transitions in the iron pnictides.) To ensure the stability of the free-energy expansion, w has to be positive. If $u > 0$ as well, we have a second-order transition. If $u < 0$, we have a first-order transition. In this case, the ratio $-u/w$ determines how strong the first-order transition is, i.e. what is the magnitude of the jump of the order parameter. For $u > 0$, we have a second-order phase transition at $r = 0$ for $h = 0$. The effect of a small but finite h is to extend the region of finite φ asymptotically to $r \to \infty$, giving rise to a "tail" in the plot of φ as function of temperature (see Fig. 5.9). Formally, there is no strict T_s, although experimentally there will be a temperature above which the distortion anisotropy is too small to be detected. Notice that, at T_s^0, the value of φ scales with the applied field according to $\varphi \sim h^{1/\delta}$, where $\delta = 3$ is the mean-field critical exponent. Let us consider $u < 0$, which gives rise to a first-order phase transition. As usual for first-order phase transitions, there is a coexistence region where the states with $\varphi = 0$ and $\varphi \neq 0$ are both local minima of the free energy. If we consider an adiabatic change of temperature, such that the system always chooses the global minimum, from the minimization of Eq. 5.1 it is straightforward to find that the transition takes place above T_s^0, at $\frac{r}{w} = \frac{9}{48}\left(\frac{u}{w}\right)^2$. We also find that the jump in the order parameter is $\Delta\varphi = \sqrt{\frac{-3u}{4w}}$. Therefore, the ratio $|u|/w$

controls the strength of the first-order transition. The effect of a finite field on the jump $\Delta\varphi$ will depend on the value of the ratio $h/|u|$. In Figure 5.9, we plot the temperature evolution of φ for different values of $|u|/w = \{1,\ 0.5,\ 0.1\}$, keeping $h/w = 0.01$ constant. The dashed line shows the magnitude of the jump $\Delta\varphi$ for $h = 0$. Notice that when the first-order transition is stronger, the jump is barely affected by the finite field. In particular, above the temperature where the jump takes place, the order parameter is never zero but is always very small, giving rise to a rather small "tail". On the other hand, when the first-order transition is weaker, the same field can completely smear out the jump. This gives rise to a noticeable and continuous "tail", and therefore to a second-order transition [45].

This analysis suggests that the anisotropy above the second order transition originates from the fact that the orthorhombic transition is actually not strictly defined in the strained (and thus orthorhombically distorted) tetragonal phase under uniaxial stress. On the other hand it suggests that the susceptibility to stress is notably enhanced in case of a weak second order transition character. We would also like to note an alternate theory was suggested [46] in which the order of the transitions could be determined by comparing the temperature of the structural transition to the critical temperature of a spin density wave state due to their linear-quadratic coupling in the Landau free energy.

I would again like to acknowledge Rafael Fernandes for developing the phenomenological model of the effect of uniaxial strain.

5.6 Conclusions of Chapter 5

Systematic characterization of the effect of permanently applied stress on the properties of $BaFe_2As_2$ using x-ray, polarized optics and electrical resistivity measurements suggest that the applied stress is actually the cause of the resistivity anisotropy in the nominally tetragonal phase. Thus the resistivity anisotropy "tail" above the tempera-

ture of the structural transition is solely due to the effect of the uniaxial strain applied to detwin the samples. This point is reinforced by the data in Chapter 4, on $SrFe_2As_2$, which the transition is strongly first order and the resistivity does not show this "tail" in the presence of strain (also see Ref. [32]). The difference between AFe_2As_2 compounds with various alkali earth metals is determined by the character and the strength (order parameter jump) of the structural transition. These conclusions are supported by a phenomenological model of the effect of the uniaxial strain on the structural transition, similar to the effect of a magnetic field on Ising ferromagnets. It is interesting to notice that this strong susceptibility to the effect of strain is also found in the orbital splitting in ARPES measurements ([47], [48]), and in the temperature dependence of the shear modulus in ultrasonic experiments [49].

CHAPTER 6. $Ba_{1-x}K_xFe_2As_2$ Resistivity Anisotropy as Evidence for a Spin Fluctuation Scattering Model

6.1 Summary of Results from $Ba_{1-x}K_xFe_2As_2$

In the $BaFe_2As_2$ family, most of the studies on its in-plane resistivity anisotropy have focused on the parent and electron-doped compounds, finding $\varrho > 0$ in both magnetic and nematic phases [30; 27; 34]. More recently, experiments in underdoped $Ba_{1-x}K_xFe_2As_2$ found a rather small, but still positive, value of ϱ [35].

This chapter reports that for larger K-doping levels, not explored in the previous studies, the anisotropy ϱ changes sign both near T_s (nematic phase) and at very low temperatures (magnetically ordered phase). Since the sign of φ is fixed by the small applied uniaxial strain, the coupling parameter κ must change sign across the magnetic/nematic dome. We interpret this sign-change as a result of asymmetric changes in the magnetic scattering and in the magnetically reconstructed band structure for electron and hole doping. This unique complexity of the nematic dome observed in the iron pnictides suggests that spin-scattering dominates transport in the normal state, establishing a possible connection to a magnetically mediated mechanism of superconductivity.

6.2 Experimental

Single crystals of $Ba_{1-x}K_xFe_2As_2$ with a size up to 7x7x1 mm^3 were grown from FeAs flux as described in Ref [36]. The potassium content in the samples was determined using electron probe microanalysis with wavelength dispersive spectroscopy (WDS), see

Ref [37] for details. Samples, had typical dimensions of 0.5 mm wide, 2 to 3 mm long and 0.05 mm thick, and were cut from cleaved slabs along the tetragonal [110] direction (which becomes either the orthorhombic a_o or b_o axis below T_{SM}). Optical imaging was performed on the samples while mounted on a cold finger in a continuous flow liquid helium cryostat (allowing for precise temperature control in 5K to 300K range) using a Leica DMLM microscope.

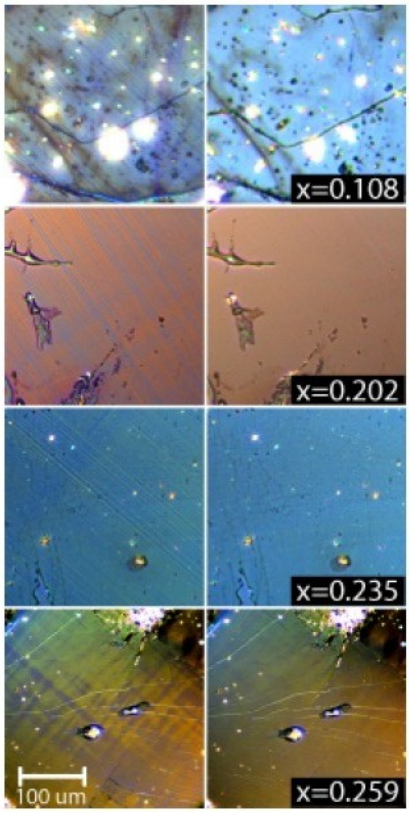

Figure 6.1 Polarized light microscopy of $Ba_{1-x}K_xFe_2As_2$ samples with doping levels x=0.108, 0.202, 0.235, 0.259, from top to bottom. Images were taken at temperatures just above the tetragonal-to-orthorhombic structural transition ($T>T_s$, right) and 5K ($T<T_s$, left), the latter showing formation of structural domains due to four different orientations of a_O and b_O axes. The difference in color of the domains is due to spectral dependence of bireflectance, depending on angle between the a_O direction and the polarization plane of incident white light. Since bireflectance is proportional to the orthorhombic distortion, the contrast naturally vanishes in the tetragonal phase (right panels). The scale bar is 100 μm.

Polarized light microscopy was used for visualization of the structural domains and the sample selection was based on the clarity of domains in the image. In Fig. 6.1 we show polarized light images of the area between potential contacts in $Ba_{1-x}K_xFe_2As_2$ crystals used in this study, with x=0.108 (non-superconducting), x=0.202 (T_c=10K), x=0.235 (T_c=26K) and x=0.259 (T_c=28K). Images were taken on cooling at a temperature slightly above T_s and at base temperature. The highest contrast is observed when the sample is aligned with the [100] tetragonal direction at a 45^o to the polarization direction of incident light (parallel and perpendicular to the orthorhombic a_o in different domains.) The contrast of domain images depends on the quality of the surface and the homogeneity of the samples. Domains are observed for samples with $x \approx 0.26$, and are no longer observed for samples with a higher doping level, x=0.34, which also do not show any features associated with structural transition in $\rho(T)$.

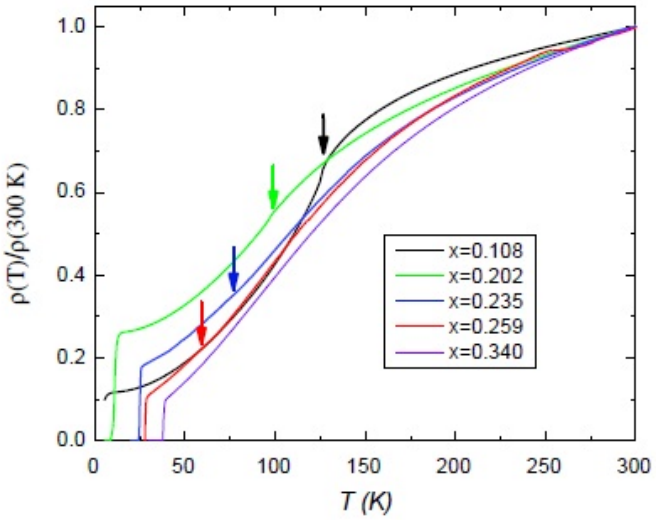

Figure 6.2 Temperature-dependent resistivity along the orthorhombic a_o-axis, ρ_a for samples of $Ba_{1-x}K_xFe_2As_2$ with four different potassium doping levels in the strain-free, twinned, state. The curves are shown using normalized plots, $\rho(T)/\rho(300K)$. Arrows indicate the transition temperatures and were determined by the maximum in the derivative of the resistivity and from polarized optical microscopy.

Selected samples were mounted for four-probe electrical resistivity measurements,

with contacts made by soldering 50 μm Ag wires using low-resistance Sn soldered contacts . Initial resistivity measurements on each sample were carried out using a flexible wire arrangement with no strain applied to the sample (free standing state). The results are plotted in Fig. 6.2. Since these measurements are performed in the twinned state of the sample and contain contributions from both components of the in-plane resistivity in the orthorhombic phase, we call it ρ_t. Samples were then mounted on a brass horseshoe straining device, and strain was applied through the voltage contact wires by deformation of the horseshoe. Strain in this configuration is applied along the tetragonal [110] axis, which selects the orthorhombic a_o axis as a preferable direction upon cooling below T_s. The strain was incrementally increased, and for each increment, temperature dependent resistivity measurements were made and the domain structure was imaged to determine the completeness of detwinning. Our previous studies using X-ray diffraction have shown that when crystals are strained to the point at which no domains are visible in polarized microscopy, about 90 % of the whole bulk of the sample represents the domain whose orthorhombic a_O axis is oriented along the direction of the strain and therefore parallel to the current. Therefore in the detwinned state we are predominantly measuring the a_o axis resistivity, ρ_{ao}, while in the unstrained state of the sample roughly equal contributions of both resistivity components are measured. Therefore, we may calculate the b_o axis resistivity, ρ_b(T)=2ρ_t(T) - ρ_a(T).

6.3 Results

Figure 6.3 presents the most important experimental finding in this chapter, the sign reversal of the in-plane resistivity anisotropy. For $Ba_{1-x}K_xFe_2As_2$ samples with $x \leq 0.202$, the resistivity is larger along the shorter orthorhombic axis, $\rho_a < \rho_b$, whereas for samples with $x \geq 0.235$, the longer axis has higher resistivity, $\rho_{\mathrm{a}} > \rho_{\mathrm{b}}$. This is clearly seen in the inset zooming in on the structural transition region. It is also apparent that,

due to the applied uniaxial strain, the in-plane anisotropy starts to appear well above the structural transition T_S of the unstrained sample.

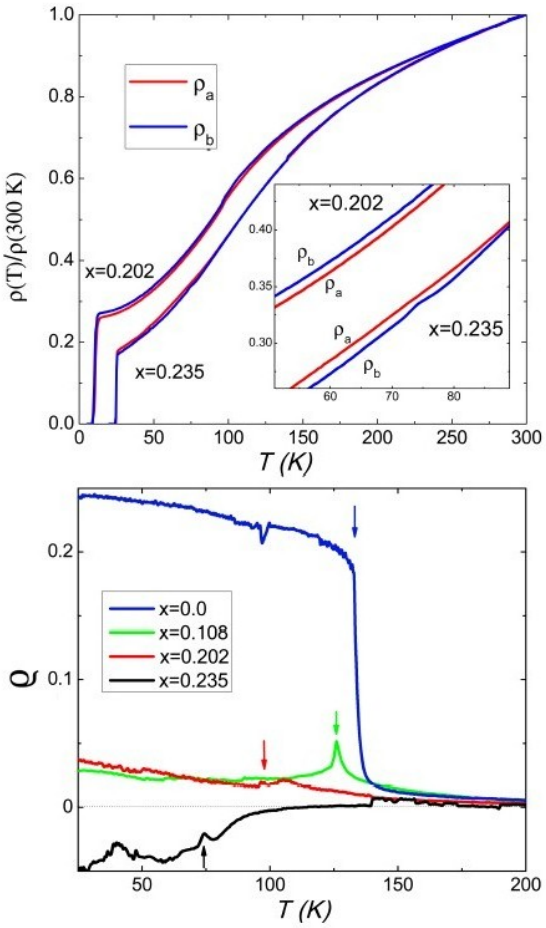

Figure 6.3 Upper panel: Normalized temperature-dependent resistivity, $\rho(T)/\rho(300K)$, for the $Ba_{1-x}K_xFe_2As_2$ samples with $x = 0.202$ and $x = 0.235$. The red lines show the resistivity along the a_o-axis (ρ_a) while the blue lines show ρ_b. The inset zooms at the structural transition, where a clear reversal of the anisotropy from $\rho_b > \rho_a$ for $x = 0.202$ to $\rho_b < \rho_a$ for $x = 0.235$ occurs. Lower panel: temperature dependence of ϱ for different K-doping levels. The arrows mark the magnetic transition temperatures.

In the bottom panel of Fig. 6.3 we plot the temperature-dependent anisotropy ratio, ϱ, for several compositions. We use two characteristic features of the $\varrho(T)$ curves to further analyze the data. First, we plot in the bottom panel of Fig. 6.4 the maximum in-plane anisotropy ϱ_{max} for different x. In the upper panel of Fig. 6.5, we plot $\varrho(T \approx T_N)$,

i.e. at temperatures immediately below the magnetic transition, which coincides with the structural transition temperature of the unstrainned $Ba_{1-x}K_xFe_2As_2$ samples.

This sign-change happens at all temperatures, even near T_N, as shown in the bottom panel of Fig. 6.3 and in the upper panel of Fig. 6.5. Furthermore, as it can be seen in the bottom panel of Fig. 6.3, the magnitude of the temperature-dependent anisotropy ratio, $\varrho(T)$, is maximal close to T_N in the parent and slightly hole-doped compositions, but increases monotonically on cooling for higher hole doping levels. This signals that the low-temperature anisotropic reconstruction of the band structure due to long-range magnetic order plays a progressively more important role near the hole-doped edge of the nematic/magnetic dome.

6.3.1 Electron vs. Hole Doping

An interesting general picture emerges from the analysis of the experimental observations of this and previous studies [30; 27; 35]. On the one hand, for all electron-doped $Ba(Fe_{1-x}Co_x)_2As_2$ and parent compositions, the resistivity anisotropy is positive, $\varrho(x) > 0$. The maximum anisotropy, $\varrho_{max}(x)$, shown in the bottom panel of Fig. 6.4, is peaked at some intermediate electron doping, vanishing near the edge of the magnetic/nematic dome, due to the vanishing orthorhombic distortion. On the other hand, on the hole-doped side, $\varrho_{max}(x)$ remains positive up to moderate hole-doping, but decreases by more than one order of magnitude, from $\varrho_{max}(x = 0) \approx +0.3$ to $\varrho_{max}(x = 0.202) \approx +0.02$. Even more surprisingly, $\varrho_{max}(x)$ changes sign and exhibits a minimum at a higher hole doping concentration, $\varrho_{max}(x = 0.235) \approx -0.034$, before it eventually approaches zero close to the edge of the magnetic/nematic dome, near $x = 0.3$.

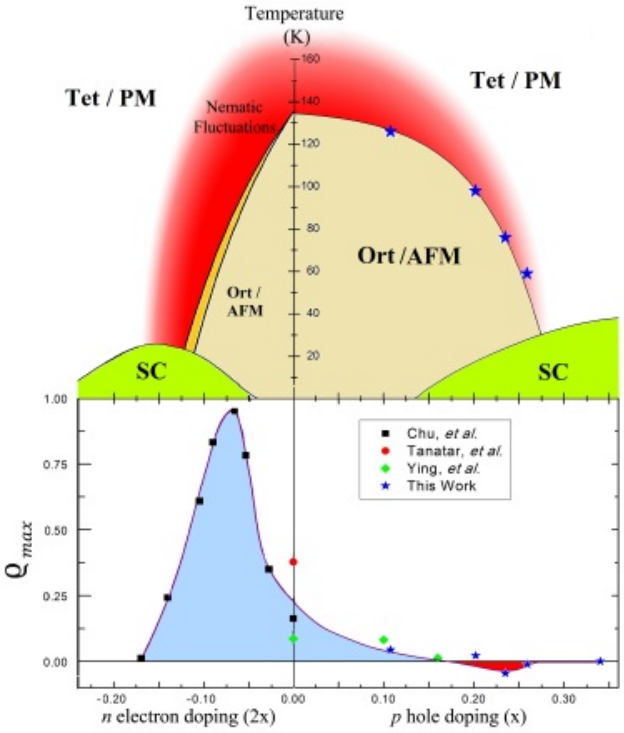

Figure 6.4 Top panel: Phase diagram of the electron- and hole-doped $BaFe_2As_2$ system focusing on the under - doped regime with the superconducting region shown in green. The region of the orthorhombic (antiferromagnetic) phase below transition from the tetragonal phase, T_S, is shown in yellow. Nematic fluctuations (red region) persist far above T_S and affect the in-plane resistivity anisotropy in strained samples. The lower panel shows the maximum in-plane anisotropy ϱ_{max} as a function of doping. Note the significant asymmetry of $\varrho_{max}(x)$ and its sign change in the hole-doped regime.

6.4 Discussion

Naively, the fact that $\rho_b > \rho_a$ across most of the phase diagram seems surprising, because the ferromagnetic direction appears to be less conducting than the antiferromagnetic one. From the orbital ordering point of view [38; 39; 40] one expects the opposite effect. However, a closer look at the Fermi surface reconstruction [27; 34] and the magnetic scattering mechanisms [41; 42] suggests that the anisotropy sign is decided by quantitative factors that depend on the electronic structure, going beyond general order

parameter arguments. Moreover, the different contributions to the transport anisotropy do not necessarily compete with each other. To sort them out, we focus first on the nematic paramagnetic phase, in which scattering by magnetic fluctuations dominates and the band structure is not yet reconstructed by the magnetic order.

The experimental doping evolution of $\varrho(T \approx T_{\mathrm{N}})$, shown in the upper panel of Fig. 6.5, displays a rather monotonic behavior, changing sign for sufficient hole-doping levels and vanishing at the edges of the nematic dome. Such a sign-change was previously predicted by the theoretical model of Ref. [41] for the anisotropic magnetic scattering in the nematic phase. The minimal model of Ref. [41], consistent with first-principles calculations, consists of a circular hole pocket at the center of the square-lattice Brillouin zone and two elliptical electron pockets centered at momenta $(\pi, 0)$ and $(0, \pi)$, which coincide with the magnetic-stripe ordering vectors. In the nematic phase, the amplitude of the fluctuations around these two ordering vectors becomes unequal [43], breaking the tetragonal symmetry of the system and inducing anisotropic scattering. In the experiment, the applied strain selects the $(\pi, 0)$ fluctuations.

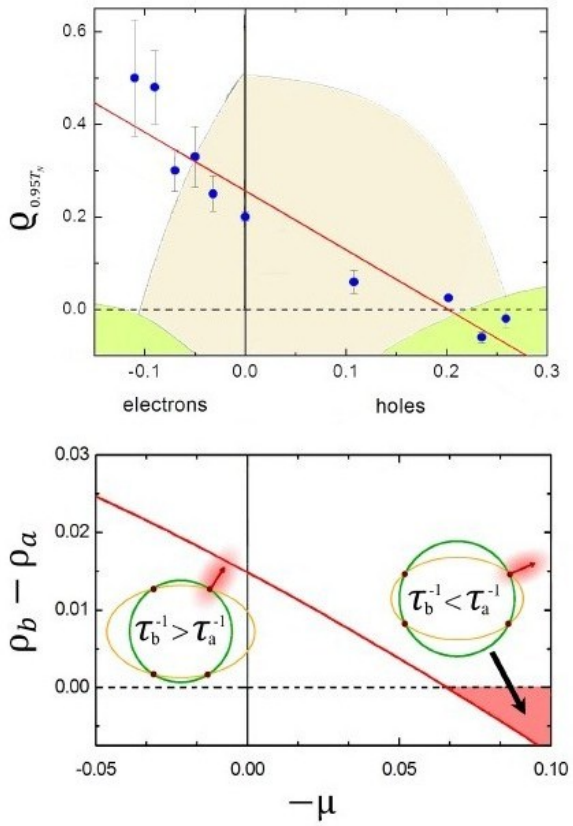

Figure 6.5 Top panel: doping dependence of the in-plane resistivity anisotropy at $0.95T_{\mathrm{N}}$ in both electron- and hole-doped $BaFe_2As_2$. The red line is a guide to the eye. The nematic/magnetic and superconducting domes are shown in the background for reference only, without a temperature scale. Bottom panel: theoretical calculation of the maximum in-plane resistivity anisotropy in the paramagnetic phase normalized by the residual resistivity, ρ_0, as a function of the change in the electron occupation number, $\Delta n/n_0$, where $n_0 = (k_F a)^2/(\pi)$. The insets schematically show the differences in the scattering rates corresponding to different Fermi velocities at the hot spots for electron- and hole-doped systems. When the hot-spot Fermi velocity has a larger component along the b (a) direction, the magnetic scattering rate is larger along the b (a) direction. The hot spots are obtained by displacing the electron pocket (yellow ellipse) by $(\pi, 0)$, making it overlap with the hole pocket (green circle). The shaded red area denotes the predicted sign reversal of the anisotropy.

CHAPTER 7. Summary, Conclusions, and Future Work

7.1 Summary

The 2008 discovery of high temperature superconductivity in iron-based compounds set off a flurry of research activity. This thesis began just before that discovery and made this new class of materials an ideal topic of study.

In Chapter 1, the motivations for understanding superconductivity were explored. As was illustrated there, these materials offer the potential for financial savings and reduced pollution, but also for furthering the progress of technology and scientific knowledge. As very little was known about this new class of iron-based materials which displayed superconductivity, the scientific community began studying every imaginable property in an attempt to capture a greater understanding of superconductivity as a whole.

These materials have a rich phase diagram in terms of both structure and magnetic ordering. Of particular interest is the coexistence of superconductivity and magnetism. These materials undergo a tetragonal to orthorhombic symmetry lowering of the crystalographic structure as well as antiferromagnetic ordering upon cooling through a characteristic temperature, T_N (see Table 2.1). This symmetry lowering results in the formation of four sets of crystalographically identical *twin* domains, but with different rotations of their axes within the orthorhombic ab-plane. Free standing samples become equally populated with a random distrobution of these twin domains which have micrometer dimensions. Bulk measurements, such as resistivity, practically speaking, require single domain samples with millimeter dimensions. Consequently the small size of these do-

mains relative to the necessary sample size prohibits any directionally dependent bulk measurement.

One of the major goals of this thesis was to study the electric anisotropy between the orthorhombic a_O and b_O axes. This meant that a sample would have to be forced into a single domain state. The $A\mathrm{Fe_2As_2}$'s (A= alkali earth) became the natural choice as their growth produced the largest and highest quality single crystals. The first obstacle was detecting these domains. X-ray diffraction is clearly the most quantitative method available, but is costly and time consuming. However, this work demonstrated that the optical properties of the domains allowed them to be viewed by polarized optical microscopy which is a much easier measurement.

Once an insight into detecting the domains was gained, research efforts were directed towards creating a method to force samples into a single domain state in the orthorhombic state. As the orthorhombic axes differ in length, it was logical to assume that in the presence of a uniaxial strain, it would become energetically more favorable for the longer orthorhomic axis (a_O) to be aligned parallel to the strain direction. To this end a straining device (nicknamed a *horseshoe* due to it's shape) was developed. This U-shaped frame could be deformed by means of a mechanical pushscrew which in turn would produce a strain in the sample, transmitted through wires soldered between the horseshoe and the sample.

It was then observed that when a sufficient strain was applied to a sample, that multiple domains were no longer visible under polarized microscopy, suggesting a single domain, *detwinned* state. This result was verified by X-ray diffraction and it was shown that samples under sufficient strain that twin domains are no longer visible have greater than 90% of their volume fraction occupied by the domain whose orthorhombic a_O axis was parallel to the strain. Samples with dimensions up to several millimeters could now be forced into a nearly single domain state, allowing for direct measurements of bulk properties along a chosen crystallograpic axis. Initial measurements on detwinned sam-

ples the parent compounds $SrFe_2As_2$, $BaFe_2As_2$, $CaFe_2As_2$, universally demonstrated a larger resistivity along the orthorhombic b_O axis than the a_O axis, with values of ρ_b/ρ_a ranging from 1.2 to 1.5.

The first detailed study in this thesis was on $SrFe_2As_2$. The resistivity anisotropy was measured for many strain values in small incrementally increasing steps leading up to the strain necessary for detwinning and then beyond. It was observed that the anistropy evolved rather dramatically with strain below the detwinning threshhold. Subsequent levels of strain had little impact on the magnitude of the anisotropy below the transition, but dramatically broadened the transition leading to a small but non-neglible anisotropy above the transition temperature, T_N. Additionally, X-ray data showed a strongly first order structural transition with the coexistence of intense Bragg peaks from both the tetragonal and orthorhombic lattices at 201K.

As $BaFe_2As_2$ was known to exhibit a second order structural transition, it was an obvious target of study to compare and contrast against the results of the strongly first order $SrFe_2As_2$. Similar to the study of the evolution of resistivity anisotropy with increasing strain in $SrFe_2As_2$, $BaFe_2As_2$ showed little change in the anisotropy below T_N. However $BaFe_2As_2$ demonstrated a much larger resistivity anisotropy above T_N than had been observed in $SrFe_2As_2$. Previous reports had attributed this as being a so called *electron nematic* phase in which the large anisotropy above the transition was intrinsic. The results of this work however, demonstrated a strong coupling between the magnitude of the strain and the resistivity anistropy above T_N. Modeling via a simple Ginzburg-Landau picture indeed suggested that the more second order the material's structural transition behaved, the stronger the anisotropy would couple to the orthorhombic distortion including that induced by the strain field. Unfortunately the question of whether or not an electronic nematic state exists remains unanswered as a measurement of the anisotropy on a detwinned sample in a strain free state has not yet been performed. This issue will be futher discussed in the Future Work section of this thesis.

Following these studies as well as other group's studies on electron-doped compounds (primarily $Ba(Fe_{1-x}Co_x)_2As_2$), a clear understanding of the source of the anisotropy had not yet been explained. As parent and electron-doped compounds had been throughly studied, hole-doped materials became an obvious direction to continue research and a study was undertaken on $Ba_{1-x}K_xFe_2As_2$. In this material, the magnitude resistivity anisotropy decreased with increasing K-doping and eventually reached zero near 20% K substitution. Interestingly, upon further doping the resistivity anisotropy redeveloped but with negative sign, that is to say: $\rho_a > \rho_b$ which was in stark contrast to all other materials peviously studied where $\rho_b > \rho_a$. This result had already been predicted in a model in which spin fluctuation scattering was the dominant source of resistivity anisotropy. A comparison of the experimental doping dependence to that predicted by the spin fluctuation scattering model shows a dramatic similarity (see Fig 6.5).

7.2 Conclusions

The goal of this thesis was to study electronic anisotropy in iron-based superconductors. This requires resistivity measurements along the orthorhombic a_O and b_O axes which cannot be made directly measured because of the formation of twin domains. Our work and results on this problem are as follows:

- In this work, it was shown that domains can be observed by polarized optical microscopy.
  - This provided a faster and less expensive way to study structural properties of samples than X-ray diffraction.
  - Most importantly for this work, it was shown that polarized microscopy can determine whether or not a sample is twinned.

- This work demonstrated that the application of uniaxial stress or strain along one of the orthorhombic axes can force a sample from a twinned state into a nearly single domain state, allowing for directional measurements of bulk properties.

- Samples of $SrFe_2As_2$, $CaFe_2As_2$, and $BaFe_2As_2$ (including daughter compounds with various chemical substitutions) were detwinned via uniaxial stress/strain allowing for successful completion of the goal of measuring in-plane electronic anisotropy in iron-based superconductors.

- The order of the structural transition was observed to have a direct impact on the nematic susceptibility of iron-based superconductors.

  - In nearly second order materials, even a small strain could produce a notible resistivity anisotropy above the structural/magnetic transition temperature.

  - Strain had little affect on the resistivity anisotropy above the transition temperature in first order materials.

- Resistivity anistoropy values ranging from $\rho_b/\rho_a = 1.2$ to 2 were observed for parent and electron-doped compounds.

  - In all parent and electron-doped samples it was observed that $\rho_b > \rho_a$

- Our study of the hole doped compound, $Ba_{1-x}K_xFe_2As_2$, revealed a dramatic asymmetry in the effects of hole vs. electron doping on resistivity anisotropy.

  - Unlike the parent and electron-doped samples where $\rho_b > \rho_a$, we demostrated that for sufficient hole doping the resistivity anisotropy changes sign such that $\rho_a > \rho_b$.

  - This result strongly corroborated theoretical preditions of a model where spin fluctuation scattering is the primary source of the electronic anisotropy within the orthorhombic ab-plane.

7.3 Future Work

The data produced while undertaking this work, most strongly corroborate with a picture in which spin fluctuation scattering plays the dominant role in the source of the resistivity anisotropy. This picture could be even more firmly solidified by studying materials with different magnetic structures. One candidate for such a study is the iron-chalcogenides. Several FeTe compounds show a similar tetragonal to orthorhombic structural symmetry lowering upon cooling, however they display dramatically different magnetic ordering. Consequently if resistivity anisotropy data matched theoretical predictions for a spin fluctuation scattering dominated model in a system with the FeTe magnetic ordering, it would provide very strong evidence, solidifying the validity of this model. However this material is technically very different from the $A\mathrm{Fe_2As_2}$ system and indeed attempts to detwin FeTe via uniaxial strain were made during this thesis study, but the results have so far been unsuccessful raising the question of whether the material can be detwinned by strain. Another option would be to magnetically detwin FeTe and would be an excellent project for future studies.

It has been clearly demonstrated that the magnitude of the anisotropy above T_N is coupled with the magnitude of the strain field. However, it remains unclear to what degree (if any) the anisotropy above T_N is intrinsic and would exist without the presence of stress or strain. We have constructed an apparatus to apply and release stress or strain *in-situ*. Although we have successfully detwinned several different materials *in-situ*, we have only produced one sample (Ru doped $\mathrm{BaFe_2As_2}$) which remained detwinned after the stress was released. No doubt the situation becomes even more complicated after attaching leads for a resistivity measurement. However the initial success should at least leave an optimistic impression that with further work, a resistivity anisotropy measurement on a detwinned, but no longer strained sample is feasible and will answer this question once and for all.

BIBLIOGRAPHY

[1] M. Hilrose, Y. Yamada, T Masuda, K. Sato, R. Hata. *SEI Technical Review* **62**, (2006).

[2] H. K. Onnes. *Proc. R. Netherlands Acad. Arts Sci. (KNAW)* **10** , 445 (1908).

[3] H. K. Onnes. *Commun. Phys. Lab, Univ. Leiden* **12**, 120 (1911).

[4] H. K. Onnes. *Proc. R. Netherlands Acad. Arts Sci. (KNAW)* **16**, 113 (1913).

[5] W. Meissner and H. Franz. *Mitteilung*, 558-559 (1930).

[6] A. Schilling, M. Cantoni, J. D. Guo, and H. R. Ott. *Nature* **363**, 56-58 (1993).

[7] Y. Kamihara, T. Watanabe, M. Hirano, and H. Hosono *Journal of the American Chemical Society* **130** 11 (2008).

[8] J. Giapintzakis, D. M. Ginsberg, P. -D. Han. *Journal of Low Temperature Physics* **77**, 1 (1989).

[9] Y. Kamihara, H. Hiramatsu, M. Hirano, R. Kawamura, H. Yanagi, T. Kamiya, and H. Hosono. *Journal of the American Chemical Society* **128** 31 (2006).

[10] M. Rotter, M. Tegel, and D. Johrendt. *Physical ReviewB* **78**, 020503(R) (2008).

[11] M. Pfisterer, G. Nagorsen. *Zeitschrift für Naturforschung B* **35**, 703 (1980).

[12] M. Pfisterer and G. Nagorsen. *Zeitschrift für Naturforschung B* **38**, 811 (1983).

[13] N. Ni, S. Nandi, A. Kreyssig, A. I. Goldman, E. D. Mun, S. L. Bud'ko, and P. C. Canfield *Physical ReviewB* **78**, 014523 (2008).

[14] S. Rozsa and H. U.Schuster. *Zeitschrift für Naturforschung B* **36**, 1668 (1981).

[15] Q. Huang, Y. Qiu, W. Bao, M. A. Green, J. W. Lynn, Y. C. Gasparovic, T. Wu, G. Wu, and X. H. Chen, Phys. *Physical Review Letters* **101**, 257003 (2008).

[16] A. I. Goldman, D. N. Argyriou, B. Ouladdiaf, T. Chatterji, A. Kreyssig, S. Nandi, N. Ni, S. L. Bud'ko, P. C. Canfield, R. J. McQueeney *Physical Review B* **78**, 100506 (2008).

[17] Y. Xiao, Y. Su, M. Meven, R. Mittal, C. M. N. Kumar, T. Chatterji, S. Price, J. Persson, N. Kumar, S. K. Dhar, Thamizhavel, Th. Brueckel

[18] J.-Q. Yan, A. Kreyssig, S. Nandi, N. Ni, S. L. Bud'ko, A. Kracher, R. J. McQueeney, R. W. McCallum, T. A. Lograsso, A. I. Goldman, and P. C. Canfield. *Physical Review B 78* , 024516 (2008).

[19] M. Rotter, M. Tegel, and D. Johrendt *Physical Review Letters* **101**, 107006 (2008).

[20] N. Ni, M. E. Tillman, J.-Q. Yan, A. Kracher, S. T. Hannahs, S. L. Bud'ko, P. C. Canfield. *Physical Review B* **78**, 214515 (2008).

[21] R. M. Fernandes, D. K. Pratt, W. Tian, J. Zarestky, A. Kreyssig, S. Nandi, M. G. Kim, A. Thaler, N. Ni, P. C. Canfield, R. J. McQueeney, J. Schmalian, and A. I. Goldman. *Physical Review B* **81**, 140501(R) (2010).

[22] S. Nandi, M. G. Kim, A. Kreyssig, R. M. Fernandes, D. K. Pratt, A. Thaler, N. Ni, S.L. Bud'ko, P. C. Canfield, J. Schmalian, R.J. McQueeney, and A.I. Goldman. *Physical Review Letters* **104**, 057006 (2010).

[23] A. S. Sefat, R. Jin, Mi. A. McGuire, B. C. Sales, D. J. Singh, D. Mandrus. *Physical Review Letters* **101**, 117004 (2008).

[24] M. J. Buerger. *American Mineralogist* **30**, 469-482 (1945).

[25] M. A.Tanatar, R. Prozorov, N. Ni, S. L. Bud'ko, P. C. Canfeld. U.S. Patent 8,450,246.

[26] M. A. Tanatar, A. Kreyssig, S. Nandi, N. Ni, S. L. Bud'ko, P. C. Canfield, A. I. Goldman, and R. Prozorov. *Physics Review B* **79**, 180508(R) (2009).

[27] M. A. Tanatar, E. C. Blomberg, A. Kreyssig, M. G. Kim, N. Ni, A. Thaler, S. L. Bud'ko, P. C. Canfield, A. I. Goldman, I. I. Mazin and R. Prozorov. *Physical Review B* **81**, 184508 (2010).

[28] S. R. Saha, N. P. Butch, K. Kirshenbaum, and J. Paglione. *Physical Review Letters* **103**, 037005 (2009).

[29] M. A. Tanatar, N. Ni, G. D. Samolyuk, S. L. Bud'ko, P. C. Canfield, and R. Prozorov. *Physical Review B* **79**, 134528 (2009).

[30] J-H. Chu, J. G. Analytis, K. De Greve, P. L. McMahon, Z. Islam, Y. Yamamoto, and I. R. Fisher. *Science* **329**, 824 (2010).

[31] T. Liang, M. Nakajima, K. Kihou, Y. Tomioka, T. Ito, C.H. Lee, H. Kito, A. Iyo, H. Eisaki, T. Kakeshita, S. Uchida. *Journal of Physics and Chemistry of Solids* **72**, 418 (2011).

[32] E. C. Blomberg, M. A. Tanatar, A. Kreyssig, N. Ni, A. Thaler, Rongwei Hu, S. L. Budḱo, P. C. Canfield, A. I. Goldman, R. Prozorov *Physical Review B* **83**, 134505 (2011).

[33] M. G. Kim, R. M. Fernandes, A. Kreyssig, J. W. Kim, A. Thaler, S. L. Bud'ko, P. C. Can
eld, R. J. McQueeney, J. Schmalian, and A. I. Goldman *Physics Review B* **83**, 134522 (2011).

[34] T. Terashima, N. Kurita, M. Tomita, K. Kihou, C.-H. Lee, Y. Tomioka, T. Ito, A. Iyo, H. Eisaki, T. Liang, M. Nakajima, S. Ishida, Shin-ichi Uchida, H. Harima, and S. Uji. *Physical Review Letters* **107**, 176402 (2011).

[35] J. J. Ying, X. F. Wang, T. Wu, Z. J. Xiang, R. H. Liu, Y. J. Yah, A. F. Wang, M. Zhang, G. J. Ye, P. Cheng, J. P. Hu, X. H. Chen. *Physical Review Letters* **107**, 067001 (2011).

[36] H. Q. Luo, Z. S. Wang, H. Yang, P. Cheng, X. Zhu, and H.-H. Wen. *Superconductor Science and Technology* **21**, 125014 (2008).

[37] M. A. Tanatar, E. C. Blomberg, Hyunsoo Kim, Kyuil Cho, W. E. Straszheim, Bing Shen, Hai-Hu Wen, R. Prozorov. *arXiv:1106.0533*.

[38] E. Bascones, M.J. Calderon, and B. Valenzuela. Low Magnetization and Anisotropy in the Antiferromagnetic State of Undoped Iron Pnictides. Phys. Rev. Lett. **104**, 227201 (2010)

[39] C.-C. Chen, J. Maciejko, A. P. Sorini, B. Moritz, R. R. P. Singh, and T. P. Devereaux. Orbital order and spontaneous orthorhombicity in iron pnictides. Phys. Rev. B **82**, 100504 (2010).

[40] W. Lv and P. Phillips. Orbitally and magnetically induced anisotropy in iron-based superconductors. Phys. Rev. B **84**, 174512 (2011).

[41] R. M. Fernandes, E. Abrahams, and J. Schmalian. *Physical Review Letters* **107**, 217002 (2011).

[42] S. Liang, G. Alvarez, C. Sen, A. Moreo, and E. Dagotto. Anisotropy of Electrical Transport in Pnictide Superconductors Studied Using Monte Carlo Simulations of the Spin-Fermion Model. Phys. Rev. Lett. **109**, 047001 (2012).

[43] R. M. Fernandes, A. V. Chubukov, J. Knolle, I. Eremin, and J. Schmalian. Preemptive nematic order, pseudogap, and orbital order in the iron pnictides. Phys. Rev. B **85**, 024534 (2012).

[44] A. Cano, M. Civelli, I. Eremin, and I. Paul, *Physical Review B* **82**, 020408(R) (2010).

[45] A. J. Millis, *Physical Review B* **81**, 035117 (2010).

[46] M. Nunez-Regueiro *Europhysics Letters* **88**, 37004 (2009).

[47] M. Yi, D. Lu, J.-H. Chu, J. G. Analytis, A. P. Sorini, A. F. Kemper, B. Moritz, S.-K. Mo, R. G. Moore, M. Hashimoto, W. S. Lee, Z. Hussain, T. P. Devereaux, I. R. Fisher, and Z.-X. Shen, *Procedings of the National Academies of Science* **108**, 6878 (2011).

[48] Y. Kim, H. Oh, C. Kim, D. Song, W. Jung, B. Kim, H. J. Choi, C. Kim, B. Lee, S. Khim, H. Kim, K. Kim, J. Hong, and Y. Kwon, *Physics Review B* **83**, 064509 (2011).

[49] R. M. Fernandes, L. H. VanBebber, S. Bhattacharya, P. Chandra, V. Keppens, D. Mandrus, M. A. McGuire, B. C. Sales, A. S. Sefat, and J. Schmalian. *Physical Review Letters* **105**, 157003 (2010).